

Monostatic Sensing with OFDM under Phase Noise: From Mitigation to Exploitation

Musa Furkan Keskin, *Member, IEEE*, Henk Wymeersch, *Senior Member, IEEE*, and Visa Koivunen, *Fellow, IEEE*

Abstract—We consider the problem of monostatic radar sensing with orthogonal frequency-division multiplexing (OFDM) joint radar-communications (JRC) systems in the presence of phase noise (PN) caused by oscillator imperfections. We begin by providing a rigorous statistical characterization of PN in the radar receiver over multiple OFDM symbols for free-running oscillators (FROs) and phase-locked loops (PLLs). Based on the delay-dependent PN covariance matrix, we derive the hybrid maximum-likelihood (ML)/maximum a-posteriori (MAP) estimator of the deterministic delay-Doppler parameters and the random PN, resulting in a challenging high-dimensional nonlinear optimization problem. To circumvent the nonlinearity of PN, we then develop an iterated small angle approximation (ISAA) algorithm that progressively refines delay-Doppler-PN estimates via closed-form updates of PN as a function of delay-Doppler at each iteration. Moreover, unlike existing approaches where PN is considered to be purely an impairment that has to be mitigated, we propose to exploit PN for resolving range ambiguity by capitalizing on its delay-dependent statistics (i.e., the range correlation effect), through the formulation of a parametric Toeplitz-block Toeplitz covariance matrix reconstruction problem. Simulation results indicate quick convergence of ISAA to the hybrid Cramér-Rao bound (CRB), as well as its remarkable performance gains over state-of-the-art benchmarks, for both FROs and PLLs under various operating conditions, while showing that the detrimental effect of PN can be turned into an advantage for sensing.

Index Terms— OFDM, joint radar-communications, phase noise, exploitation, iterated small angle approximation.

I. INTRODUCTION

Envisioned as one of the key enabling technologies in 6G wireless networks, the concept of joint radar-communications (JRC), also known as integrated sensing and communications (ISAC), has drawn significant attention in recent years [1]–[6]. Towards practical JRC implementation in real-world scenarios, two principal design paradigms have been pursued in the literature: radar-communications coexistence (RCC) [7] and dual-functional radar-communications (DFRC) [8], [9]. RCC deals with joint optimization of spectrally coexisting radar and communication systems deployed on separate platforms to mitigate mutual interference and enable efficient spectrum utilization [10], while DFRC refers to integration of sensing and communication functionalities into a single hardware that employs a joint waveform to perform both tasks simultaneously for mutual benefit [4]. Sparking innovative use cases (e.g., sensing-assisted communications [6]) and bringing hardware/cost efficiency by piggybacking on the existing wireless infrastructure, DFRC holds great potential in emerging 6G networks, where sensing will be an integral component [6], [11]. As a promising candidate for DFRC transmission, the orthogonal frequency-division multiplexing (OFDM) waveform has been extensively studied thanks to its wide prevalence in mobile network standards and its satisfactory performance in radar operation [12]–[15].

Musa Furkan Keskin and Henk Wymeersch are with the Department of Electrical Engineering, Chalmers University of Technology, SE 41296 Gothenburg, Sweden (e-mail: furkan@chalmers.se). Visa Koivunen is with the Department of Signal Processing and Acoustics, Aalto University, FI 00076 Aalto, Finland. This work is supported, in part, by MSCA-IF grant 888913 (OTFS-RADCOM) and the European Commission through the H2020 project Hexa-X (Grant Agreement no. 101015956).

As next-generation wireless systems are expected to operate at high frequencies, i.e., millimeter wave (mmWave) bands [11], hardware impairments (HWIs), such as phase noise (PN) [16], power amplifier nonlinearity (PAN) and mutual coupling (MC), can become a major bottleneck for OFDM DFRC system performance in both radar and communications [17], [18]. In particular, the severity of PN, which is caused by oscillator imperfections¹, increases with operating frequency [19], [21]. Due its rapidly time-varying nature, PN requires dynamic compensation accounting for subcarrier-level (frequency-domain) or sample-level (time-domain) mitigation processing, thereby posing a significant challenge in channel estimation and data detection for OFDM communications [19], [22]–[24]. To tackle the PN compensation problem for OFDM, various frequency-domain [21], [25]–[28] and time-domain [16], [29], [30] estimation approaches have been proposed.

Despite the vast literature on PN estimation in *OFDM communications*, very little effort has been devoted to studying the impact of PN on the performance of *OFDM radar* (e.g., [31], [32]), let alone to developing algorithms to estimate and compensate for PN in radar sensing. In [31] and [32], the effect of PN on the range-velocity profile of an OFDM radar is investigated, which shows that PN leads to an increase in noise floor and produces a ridge along the velocity axis. To support new use cases towards 6G networks, emerging mmWave sensing applications [33]–[36] impose stringent requirements on range and velocity accuracy [37], which necessitates the consideration of PN. From the perspective of radar receive processing, the existing OFDM radar algorithms (e.g., [12], [14], [38]–[41]) assume ideal oscillators and thus cannot provide satisfactory performance under the effect of PN, especially for large PN variances. In a nutshell, no systematic study has been performed to tackle the problem of radar sensing in OFDM DFRC systems with oscillator PN, and, accordingly, to derive an algorithm to jointly estimate delay, Doppler and PN.

As a key distinction between radar and communications, the so-called *range correlation* effect [42]–[45] constitutes an essential peculiarity of PN in monostatic radar sensing compared to PN in a communications setup. Due to independent PN processes at the transmitter and the receiver, the PN statistics in communications systems do not depend on unknown channel parameters (e.g., [16], [19], [46], [47]). Conversely, in a shared-oscillator radar transceiver, down-conversion of the reflected signal from a target results in a differential (self-referenced/self-correlated) PN process [48], [49] corresponding to the difference between the original PN process and its version shifted in time by the round-trip delay of the target. This correlation effect renders the statistics of PN in the radar receiver range-dependent, leading to higher PN variance for farther targets [43], which brings both challenges and opportunities specific to radar sensing. The main

¹Being a time-varying impairment, PN constitutes a much more serious issue for DFRC systems than static impairments caused by oscillator non-idealities, such as carrier frequency offset (CFO) and I/Q imbalance [19]. For instance, CFO has no effect on monostatic sensing systems as the same oscillator is employed for transmission and reception [20].

challenge pertains to delay and PN being coupled, making it difficult to disentangle the corresponding estimation tasks (as is commonly performed in joint channel/PN estimation in OFDM communications, e.g., [29], [50]). On the other hand, the main opportunity arises from the possibility to exploit the range-dependent PN statistics for enhancing range estimation performance. While *PN exploitation* may offer promising performance gains, to the best of authors' knowledge, this topic remains surprisingly unexplored, both in the standard radar literature (i.e., frequency-modulated continuous wave (FMCW), multiple-input multiple-output (MIMO) or pulsed radars) and in OFDM DFRC research.

In light of the existing literature, several fundamental questions arise concerning the sensing functionality of OFDM DFRC systems in the presence of PN:

- What are the statistical properties of PN in the OFDM radar receiver for different types of oscillators, namely, free-running oscillators (FROs) and phase-locked loops (PLLs) [25], [48]?
- How can we develop powerful algorithms for joint estimation of delay, Doppler and PN, to *mitigate* the impact of PN on the sensing performance? How do FROs and PLLs affect the performance of delay and Doppler estimation?
- Considering the range correlation effect, is it possible to *exploit* PN to improve ranging performance beyond that achievable via PN-free, ideal oscillators?

In an attempt to answer these questions, this paper studies the problem of radar delay-Doppler estimation in OFDM DFRC systems in the face of oscillator PN. We begin by deriving the statistical characteristics of PN in the OFDM radar observations for both FROs and PLLs. Then, we propose a novel algorithm for joint estimation of delay, Doppler and PN, based on iterated small angle approximation of PN in the cost function of the hybrid maximum-likelihood (ML)/MAP estimator, which enables fast convergence to the corresponding theoretical bounds. Furthermore, we develop a PN exploitation approach that can effectively utilize the delay-dependent PN statistics to resolve range ambiguity. The main contributions of this paper can be summarized as follows:

- **Problem Formulation for OFDM Radar Sensing under PN:** For the first time in the literature, we investigate the problem of monostatic radar sensing in OFDM DFRC systems under the effect of oscillator PN. To provide a rigorous problem formulation, we derive an explicit statistical characterization of PN in the OFDM radar receiver. We consider two commonly used oscillator models, namely, FRO and PLL. The derivations reveal the block-diagonal structure of the PN covariance matrix for the former and the more general Toeplitz-block Toeplitz structure for the latter.
- **Hybrid ML/MAP Estimator via Iterated Small Angle Approximation Algorithm:** We derive the hybrid ML/MAP estimator of the deterministic delay-Doppler parameters and the random PN over an OFDM frame with multiple symbols. The covariance matrix of PN in the backscattered signal depends on the unknown delay. To deal with the highly nonlinear nature of the resulting cost function, we propose a novel iterated small angle approximation (ISAA) approach that invokes the small PN approximation around the current PN estimate at each iteration, progressively refining delay-Doppler-PN estimates and minimizing the impact of residual PN. The proposed approach enables closed-form update of PN as a function of delay-Doppler and provides significant improvements in PN tracking accuracy through alternating iterations.

- **PN Exploitation to Resolve Range Ambiguity:** Relying on the key insight that PN conveys valuable information on delay through its delay-dependent statistics, we develop an algorithm for resolving range ambiguity, that exploits the statistics of the PN estimates at the output of the proposed ISAA method. The PN exploitation approach formulates the range estimation as a parametric covariance matrix reconstruction problem by leveraging the Toeplitz-block Toeplitz structure and is capable of yielding unambiguous range estimates through the fact that PN covariance imposes no ambiguity in range (as opposed to the fundamental upper limit dictated by OFDM subcarrier spacing [12], [39], [51]).
- **Simulation Analysis:** Extensive simulations conducted under a wide variety of operating conditions indicate that the proposed ISAA algorithm converges quickly to the corresponding hybrid Cramér-Rao bounds (CRBs) [52], [53] on delay-Doppler-PN estimation in few iterations and considerably outperforms the benchmark FFT method [12], [39], [40]. The accuracy gains are more pronounced for higher SNRs, larger 3 dB oscillator bandwidths, smaller loop bandwidths (for PLLs) and farther targets. In addition, PLLs are found to be more beneficial for Doppler estimation than FROs, due to the presence of slow-time PN correlation for PLLs. Moreover, above a certain SNR level, the PN exploitation algorithm is shown to correctly identify the true range of range-ambiguous targets and achieve much higher ranging accuracy than the FFT method fed with PN-free observations, thereby turning PN into an advantage for sensing.²

II. SYSTEM MODEL AND PROBLEM FORMULATION

Consider an OFDM JRC system consisting of a DFRC transceiver and a communications receiver (RX), as shown in Fig. 1. Equipped with a radar-communications transmitter (TX) (i.e., a conventional OFDM TX) and a radar RX on a single hardware platform, the DFRC transceiver sends data symbols to the communications RX and simultaneously performs monostatic radar sensing using the backscattered signals to accomplish various radar tasks (e.g., target detection, estimation, tracking and classification) [2], [8], [12]. To enable full-duplex operation without self-interference to the radar RX, we assume sufficient isolation and decoupling of TX/RX antennas at the DFRC transceiver [6], [12], [39], [54]–[56]. At the communications RX, conventional OFDM receive operations (e.g., channel estimation, frequency synchronization, data detection [24]) are performed ordinarily without any constraints from the sensing functionality. Moreover, the oscillator of the DFRC transceiver, which is shared between the TX and radar RX on the co-designed joint hardware platform, is assumed to be non-ideal and impaired by PN due to imperfections [19], [21], [25], [46], [57]. In this section, we derive OFDM transmit and radar receive signal models in the presence of PN, and formulate the resulting OFDM radar sensing problem. We note that the paper will focus on radar sensing under PN while the communications RX is assumed to compensate for PN via well-established approaches, e.g., [16], [22], [30], [58].

²Notations: $\Pi_{\mathbf{X}} = \mathbf{X}(\mathbf{X}^H \mathbf{X})^{-1} \mathbf{X}^H$ represents the orthogonal projector onto the column space of \mathbf{X} and $\Pi_{\mathbf{X}}^{\perp} = \mathbf{I} - \Pi_{\mathbf{X}}$. \odot and \otimes denote the Hadamard and Kronecker product, respectively. $\text{diag}(\mathbf{x})$ outputs a diagonal matrix with the elements of a vector \mathbf{x} on the diagonals, $\text{diag}(\mathbf{X})$ represents a diagonal matrix with the diagonal elements of a square matrix \mathbf{X} on the diagonals, $\text{vec}(\cdot)$ denotes matrix vectorization operator, and $\text{reshape}_{N,M}(\cdot)$ reshapes a vector into an $N \times M$ matrix.

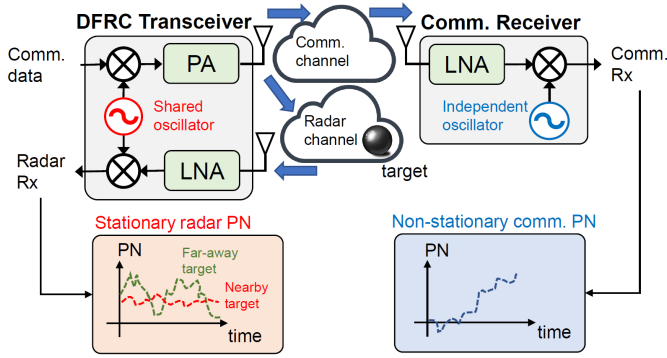


Fig. 1. OFDM JRC system comprising a DFRC transceiver that sends data symbols to a communications RX and simultaneously performs monostatic sensing using the backscattered signals under the impact of PN. Downconversion of the radar return signal using the shared oscillator results in a self-correlated PN process, leading to delay-dependent PN statistics in radar sensing, while PN statistics in the communications RX, which employs an independent oscillator, have no relation to channel parameters.

A. Transmit Signal Model

We consider an OFDM communication frame with M symbols and N subcarriers. The total duration of a symbol is given by $T_{\text{sym}} = T_{\text{cp}} + T$, where T_{cp} and T denote, respectively, the cyclic prefix (CP) and the elementary symbol durations [12]. In addition, $\Delta f = 1/T$ is the subcarrier spacing, leading to a total bandwidth of $N\Delta f = B$. The complex baseband OFDM transmit signal can be expressed as [13]

$$s(t) = \sum_{m=0}^{M-1} s_m(t), \quad (1)$$

where

$$s_m(t) = \frac{1}{\sqrt{N}} \sum_{n=0}^{N-1} x_{n,m} e^{j2\pi n \Delta f t} \text{rect} \left(\frac{t - mT_{\text{sym}}}{T_{\text{sym}}} \right) \quad (2)$$

is the OFDM signal for the m^{th} symbol, $x_{n,m}$ denotes the complex data symbol on the n^{th} subcarrier for the m^{th} symbol, and $\text{rect}(t)$ is a rectangular pulse that takes the value 1 for $t \in [0, 1]$ and 0 otherwise. In the presence of PN in the oscillator, the upconverted transmit signal over the block of M symbols for $t \in [0, MT_{\text{sym}}]$ can be written as [49]

$$\tilde{s}(t) = \Re \left\{ s(t) e^{j[2\pi f_c t + \phi(t)]} \right\}, \quad (3)$$

where f_c is the carrier frequency and $\phi(t)$ denotes the PN process in the oscillator.

B. Receive Signal Model

In radar sensing, we assume the existence of a point target in the far-field, with round-trip delay $\tau = 2R/c$, normalized Doppler shift $\nu = 2v/c$ and complex channel gain α , which includes path loss and radar cross section effects. Here, R , v and c denote the distance, radial velocity and speed of propagation, respectively. Given the transmit signal model in (3), the passband backscattered signal at the radar RX can be given as

$$\tilde{y}(t) = \Re \left\{ \alpha s(t - \tau(t)) e^{j[2\pi f_c (t - \tau(t)) + \phi(t - \tau(t))]} \right\}, \quad (4)$$

where $\tau(t) = \tau - \nu t$ is the time-varying delay due to Doppler shift. After downconverting the passband signal in (4) through the noisy oscillator, which corresponds to multiplication by $e^{-j(2\pi f_c t + \phi(t))}$ [59], the equivalent complex baseband signal can be written as [44]

$$y(t) = \alpha s(t - \tau(t)) e^{j[2\pi f_c (t - \tau(t)) + \phi(t - \tau(t))]} e^{-j[2\pi f_c t + \phi(t)]}$$

$$= \alpha s(t - \tau(t)) e^{-j2\pi f_c \tau} e^{j2\pi f_c \nu t} e^{j[\phi(t - \tau(t)) - \phi(t)]}. \quad (5)$$

Focusing primarily on vehicular JRC scenarios, we assume that the Doppler shifts satisfy $|\nu| \ll 1/N$ [14], [20], [38], where for typical vehicular OFDM JRC systems, $\nu \ll 10^{-6}$ (corresponding to $v \ll 540$ km/h), while N is on the order of 10^3 . This allows us to approximate the PN term in (5) as $\phi(t - \tau(t)) \approx \phi(t - \tau)$. In addition, the time-bandwidth product BMT_{sym} is small enough to justify (together with $|\nu| \ll 1/N$) the narrowband approximation $s(t - \tau(t)) \approx s(t - \tau)$ [51]. Under this setting, the received signal in (5) becomes

$$y(t) = \alpha s(t - \tau) e^{-j2\pi f_c \tau} e^{j2\pi f_c \nu t} w(t, \tau), \quad (6)$$

where the multiplicative PN process is represented by

$$w(t, \tau) \triangleq e^{j[\phi(t - \tau) - \phi(t)]}. \quad (7)$$

The statistical properties of the PN process $\phi(t - \tau) - \phi(t)$ in (7) will be derived in Sec. III.

C. Fast-Time/Slow-Time Representation with Phase Noise

For the m^{th} symbol, we remove the CP and sample $y(t)$ in (6) at $t = mT_{\text{sym}} + T_{\text{cp}} + \ell T/N$ for $\ell = 0, \dots, N-1$. Making the standard OFDM radar assumptions $T_{\text{cp}} \geq \tau$ [1], [38], [39] (CP duration is set to be longer than the round-trip delay of the furthest target) and $f_c T \nu \ll 1$ [15], [60]–[62] (Doppler shift $f_c \nu$ is small compared to subcarrier spacing Δf), and ignoring constant phase terms, the received signal for the m^{th} symbol can be written as [14], [20]

$$y_{\ell,m} = \alpha e^{j2\pi f_c m T_{\text{sym}} \nu} w_{\ell,m}(\tau) \times \frac{1}{\sqrt{N}} \sum_{n=0}^{N-1} x_{n,m} e^{j2\pi n \frac{\ell}{N}} e^{-j2\pi n \Delta f \tau}, \quad (8)$$

where $w_{\ell,m}(\tau)$ is the sampled version of the PN term $w(t, \tau)$ in (6) for $t = mT_{\text{sym}} + T_{\text{cp}} + \ell T/N$. Let

$$\mathbf{b}(\tau) \triangleq \left[1, e^{-j2\pi \Delta f \tau}, \dots, e^{-j2\pi (N-1) \Delta f \tau} \right]^T, \quad (9)$$

$$\mathbf{c}(\nu) \triangleq \left[1, e^{-j2\pi f_c T_{\text{sym}} \nu}, \dots, e^{-j2\pi f_c (M-1) T_{\text{sym}} \nu} \right]^T, \quad (10)$$

represent the frequency-domain and temporal (slow-time) steering vectors, respectively.

Aggregating the observations in (8) over fast-time ℓ and slow-time m , and taking into account the presence of additive sensor noise, the fast-time/slow-time observation matrix in the presence of PN is obtained as [20]

$$\mathbf{Y} = \alpha \mathbf{W} \odot \mathbf{F}_N^H \left(\mathbf{X} \odot \mathbf{b}(\tau) \mathbf{c}^H(\nu) \right) + \mathbf{Z}, \quad (11)$$

where $\mathbf{W} \in \mathbb{C}^{N \times M}$ with $[\mathbf{W}]_{\ell,m} \triangleq w_{\ell,m}(\tau)$ is the *multiplicative PN matrix*³ consisting of fast-time/slow-time samples from the PN process in (7), $\mathbf{F}_N \in \mathbb{C}^{N \times N}$ is the unitary DFT matrix with $[\mathbf{F}_N]_{\ell,n} = \frac{1}{\sqrt{N}} e^{-j2\pi n \frac{\ell}{N}}$, $\mathbf{X} \in \mathbb{C}^{N \times M}$ contains the complex data symbols with $[\mathbf{X}]_{n,m} \triangleq x_{n,m}$, $\mathbf{Y} \in \mathbb{C}^{N \times M}$ with $[\mathbf{Y}]_{\ell,m} \triangleq y_{\ell,m}$, and $\mathbf{Z} \in \mathbb{C}^{N \times M}$ is additive white Gaussian noise (AWGN) with $\text{vec}(\mathbf{Z}) \sim \mathcal{CN}(\mathbf{0}, 2\sigma^2 \mathbf{I})$. As observed from (11), the PN component \mathbf{W} introduces intercarrier interference (ICI) in OFDM radar [14], [20], [51] (similar to its effect in OFDM communications [16], [19], [21], [25]) and might severely degrade the performance of delay-Doppler estimation.

³For notational convenience, we drop the dependence of \mathbf{W} on τ .

D. Special Case: Ideal Oscillator

To relate the derived signal model in (11) to the commonly used ones in the literature, we investigate the special case of an ideal oscillator where the PN process is not present, i.e., $\phi(t) = 0, \forall t$, which yields $w(t, \tau) = 1, \forall t, \tau$, and \mathbf{W} becomes an all-ones matrix, i.e., $\mathbf{W} = \mathbf{1}_{N \times M}$. In this case, (11) reverts to the PN-free model

$$\mathbf{Y}^{\text{PN-free}} = \alpha \mathbf{F}_N^H \left(\mathbf{X} \odot \mathbf{b}(\tau) \mathbf{c}^H(\nu) \right) + \mathbf{Z}. \quad (12)$$

Following the traditional processing chain for OFDM radar receivers [12], [39], [40], we take the DFT of the columns of $\mathbf{Y}^{\text{PN-free}}$ in (12) to switch from fast-time/slow-time to frequency/slow-time domain and obtain the standard OFDM radar observations [12], [15], [39], [40], [60], [61]:

$$\tilde{\mathbf{Y}} = \mathbf{F}_N \mathbf{Y}^{\text{PN-free}} = \alpha \mathbf{X} \odot \mathbf{b}(\tau) \mathbf{c}^H(\nu) + \mathbf{F}_N \mathbf{Z}, \quad (13)$$

where $\text{vec}(\mathbf{F}_N \mathbf{Z}) \sim \mathcal{CN}(\mathbf{0}, 2\sigma^2 \mathbf{I})$. Clearly, (13) does not involve any ICI effect, and is therefore amenable to conventional delay-Doppler estimation algorithms (after removing the effect of \mathbf{X}), such as 2-D DFT over time and frequency domains [12], [39], [40] and super-resolution methods [60], [61].

E. Problem Statement for OFDM Radar under Phase Noise

Given the transmit data symbols⁴ \mathbf{X} and the fast-time/slow-time observations \mathbf{Y} in (11), the problem of interest for OFDM radar sensing in the presence of PN is to estimate the target parameters α, τ and ν , which inherently involves estimating the PN matrix \mathbf{W} and compensating for its effect on \mathbf{Y} . To tackle this problem, we first derive the statistical properties of the PN process in Sec. III, which will then be utilized in Sec. IV to propose a novel algorithm for joint estimation of delay, Doppler and PN. In Sec. V, we take a step further by exploiting PN as something beneficial for radar sensing.

III. PHASE NOISE STATISTICS

This section provides a statistical characterization of the PN process $\phi(t - \tau) - \phi(t)$ in (7), gives expressions of the PN variance for different types of oscillators and derives the structure of the PN covariance matrix.

A. Statistics of Differential Phase Noise Process

Let $\phi(t)$ be a zero-mean Gaussian random process with variance $\sigma_\phi^2(t)$ [30], [49], i.e.,

$$\phi(t) \sim \mathcal{N}(0, \sigma_\phi^2(t)), \quad (14)$$

where the form of $\sigma_\phi^2(t)$ depends on the type of oscillator. Let us define the *differential* PN (DPN) process [63] (also called *self-referenced* PN, *increment* PN process [48], or *PN variation* [49]) as

$$\xi(t, \tau) \triangleq \phi(t) - \phi(t - \tau). \quad (15)$$

Since the DPN process⁵ is stationary, its statistics depend only on the increment value (target delay) τ [48, Sec. IV]. Hence, the DPN process can be statistically characterized as [49]

$$\xi(t, \tau) \sim \mathcal{N}(0, \sigma_\xi^2(\tau)), \quad (16)$$

where $\sigma_\xi^2(\tau)$ is the delay-dependent variance of $\xi(t, \tau)$. The following lemma provides the second-order statistics of $\xi(t, \tau)$.

⁴Being co-located on a shared platform with the JRC transmitter, the radar receiver has the knowledge of transmit data symbols \mathbf{X} [12], [14], [20].

⁵While $\xi(t, \tau)$ is called the DPN here to distinguish it from the actual PN process $\phi(t)$, we will mostly refer to $\xi(t, \tau)$ as PN in the remainder of the text for ease of exposition.

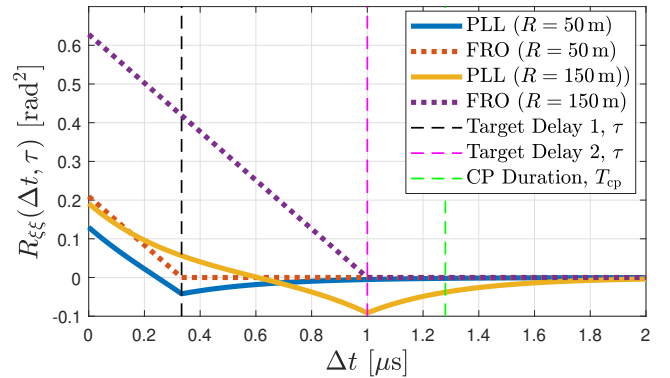


Fig. 2. Covariance of the DPN process $\xi(t, \tau)$ in (15), computed via the expression in (17), for PLL and FRO architectures at two different target ranges $R = 50$ m and $R = 150$ m, where the 3 dB bandwidth is $f_{3\text{dB}} = 50$ kHz and the PLL loop bandwidth is $f_{\text{loop}} = 500$ kHz. Contrary to OFDM communications, the PN statistics in OFDM radar depend on target delay, as also illustrated in Fig. 1.

Lemma 1. *The correlation function of the DPN process $\xi(t, \tau)$ in (15) is given by*

$$\begin{aligned} R_{\xi\xi}(\Delta t, \tau) &= R_{\xi\xi}(t_1, t_2, \tau) \triangleq \mathbb{E}[\xi(t_1, \tau)\xi(t_2, \tau)] \quad (17) \\ &= \frac{\sigma_\xi^2(\tau + \Delta t) + \sigma_\xi^2(\tau - \Delta t)}{2} - \sigma_\xi^2(\Delta t), \end{aligned}$$

where $\Delta t \triangleq t_1 - t_2$ is the time difference.

Proof. Please see Appendix A.

B. PN Variance for Different Oscillator Types

Lemma 1 allows us to compute the correlation of $\xi(t, \tau)$ in terms of its delay-dependent variance function $\sigma_\xi^2(\tau)$. We now provide expressions for $\sigma_\xi^2(\tau)$ by distinguishing between two realizations of an oscillator, namely, free-running oscillator (FRO) and phase-locked loop (PLL) synthesizer [25], [48].

1) *Free-Running Oscillators (FROs)*: For FROs, the variance of the DPN $\xi(t, \tau)$ in (16) is given by [48, Sec. V], [49, Sec. V, VI], [25, Sec. III-A]

$$\sigma_\xi^2(\tau) = 4\pi f_{3\text{dB}} |\tau|, \quad (18)$$

where $f_{3\text{dB}}$ is the 3 dB bandwidth of the Lorentzian oscillator spectrum.

2) *Phase-Locked Loop (PLL) Synthesizers*: For PLL architectures, the delay-dependent variance in (16) can be expressed as [48, Sec. VII-A], [49, Sec. III]

$$\sigma_\xi^2(\tau) = \frac{2f_{3\text{dB}}}{f_{\text{loop}}} \left(1 - e^{-2\pi f_{\text{loop}} |\tau|} \right), \quad (19)$$

where f_{loop} denotes the loop bandwidth of PLL.

We note that PLL degenerates to FRO with decreasing f_{loop} , i.e., (19) converges to (18) as $f_{\text{loop}} \rightarrow 0$. With the expressions (18) and (19), a complete statistical characterization of $\xi(t, \tau)$ can be obtained via (16) and (17) for FROs and PLLs, which, in turn, yields the covariance matrix of the fast-time/slow-time PN samples in \mathbf{W} in (11). As an example, Fig. 2 plots the covariance of $\xi(t, \tau)$ at different target delays τ for both PLLs and FROs. The figure illustrates the *delay-dependency* of the PN statistics in OFDM radar sensing (as opposed to OFDM communications, e.g., [19], [46], [47]) and provides insights into the effect of PLL based control on the correlation behavior of PN.

C. Delay-Dependent PN Covariance Matrix

Let $\mathbf{w} \triangleq \text{vec}(\mathbf{W}) \in \mathbb{C}^{NM \times 1}$ and $\boldsymbol{\xi} \in \mathbb{R}^{NM \times 1}$ be the sampled version of the PN process in (15) over the entire

OFDM frame, i.e., $\mathbf{w} = e^{-j\xi}$ from (7). Then, ξ can be statistically characterized as⁶

$$\xi \sim \mathcal{N}(\mathbf{0}, \mathbf{R}(\tau)), \quad (20)$$

where $\mathbf{R}(\tau) \in \mathbb{R}^{NM \times NM}$ is the delay-dependent positive definite covariance matrix of ξ . Using (16) and (17), the $(i_1, i_2)^{\text{th}}$ entry of $\mathbf{R}(\tau)$ can be written as

$$[\mathbf{R}(\tau)]_{i_1, i_2} = R_{\xi\xi}(\Delta t_{i_1 i_2}, \tau), \quad (21)$$

where

$$\Delta t_{i_1 i_2} \triangleq (i_1 - i_2)T_s + (m_1 - m_2)T_{\text{cp}} \quad (22)$$

for $(i_1, i_2) = (n_1 + m_1 N, n_2 + m_2 N)$, with $0 \leq n_1, n_2 \leq N - 1$ and $0 \leq m_1, m_2 \leq M - 1$ denoting the fast-time and slow-time sample indices, respectively, and $T_s = T/N$ the sampling interval. We note from (22) that due to CP removal, $\Delta t_{i_1 i_2}$ depends not only on $i_1 - i_2$, but also on the difference between symbol (slow-time) indices for PN samples belonging to different symbols.

From (21) and (22), it is straightforward to see that $\mathbf{R}(\tau)$ is a symmetric *Toeplitz-block Toeplitz* matrix [64] consisting of $M \times M$ blocks of size $N \times N$:

$$\mathbf{R}(\tau) = \begin{bmatrix} \mathbf{R}_0(\tau) & \mathbf{R}_1(\tau) & \dots & \mathbf{R}_{M-1}(\tau) \\ \mathbf{R}_1^T(\tau) & \ddots & \ddots & \\ & \ddots & \ddots & \mathbf{R}_1(\tau) \\ \mathbf{R}_{M-1}^T(\tau) & & \mathbf{R}_1^T(\tau) & \mathbf{R}_0(\tau) \end{bmatrix}, \quad (23)$$

where the m^{th} Toeplitz block $\mathbf{R}_m(\tau) \in \mathbb{R}^{N \times N}$ is given by

$$[\mathbf{R}_m(\tau)]_{n_1, n_2} = R_{\xi\xi}(\Delta t_{n_1 n_2}^{(m)}, \tau) \quad (24)$$

with $\Delta t_{n_1 n_2}^{(m)} \triangleq (n_1 - n_2)T_s - mT_{\text{sym}}$. While PLLs exhibit the generic Toeplitz-block Toeplitz structure in (23), FROs lead to a more special covariance structure, as pointed out in the following lemma.

Lemma 2. *The PN covariance matrix $\mathbf{R}(\tau)$ in (23) is block-diagonal for FROs with $\tau \leq T_{\text{cp}}$, i.e.,*

$$\mathbf{R}(\tau) = \text{blkdiag}(\mathbf{R}_0(\tau), \dots, \mathbf{R}_0(\tau)). \quad (25)$$

Proof. Please see Appendix B.

An intuitive interpretation of Lemma 2 can be provided as follows. Since PN samples in different symbols are separated in time by at least T_{cp} , the PN process in (15) with $\tau \leq T_{\text{cp}}$ becomes uncorrelated from one symbol to another. In other words, the time intervals for PN accumulation [48] corresponding to $\xi(t, \tau)$ and $\xi(t + T_{\text{cp}}, \tau)$ are non-overlapping, leading to uncorrelated PN in the absence of a control loop. This result is also corroborated by Fig. 2, where the correlation in case of FRO is zero for $\Delta t \geq \tau$, while the correlation for PLL can have non-zero values for $\Delta t \geq T_{\text{cp}}$.

IV. PROPOSED ALGORITHM FOR DELAY-DOPPLER ESTIMATION UNDER PHASE NOISE

In this section, using the statistical characterization of PN derived in (20) and (23), we formulate the sensing problem stated in Sec. II-E using a hybrid ML/MAP estimation approach and propose a novel iterated small angle approximation (ISAA) algorithm to jointly estimate delay, Doppler and PN.

⁶The derivation of PN statistics can be straightforwardly extended to the multi-target case by computing cross-correlation of PN vectors associated with different targets at different delays, following the arguments in Lemma 1.

A. Hybrid ML/MAP Estimator

To derive the hybrid ML/MAP estimator of delay, Doppler and PN, we first rewrite the observations in (11) as

$$\mathbf{y} = \alpha \Xi \mathbf{q}(\tau, \nu) + \mathbf{z}, \quad (26)$$

where $\mathbf{y} \triangleq \text{vec}(\mathbf{Y}) \in \mathbb{C}^{NM \times 1}$, $\mathbf{z} \triangleq \text{vec}(\mathbf{Z}) \in \mathbb{C}^{NM \times 1}$,

$$\Xi \triangleq \text{diag}(e^{-j\xi}) \in \mathbb{C}^{NM \times NM}, \quad (27)$$

$$\mathbf{q}(\tau, \nu) \triangleq \text{vec}\left(\mathbf{F}_N^H \left[\mathbf{X} \odot \mathbf{b}(\tau) \mathbf{c}^H(\nu) \right]\right) \in \mathbb{C}^{NM \times 1}. \quad (28)$$

Our goal herein is to estimate from (26) the unknown parameter vector $\boldsymbol{\eta} = [\tau, \nu, \alpha, \xi^T]^T$, consisting of both random (ξ) and deterministic (τ, ν, α) parameters⁷. Then, the hybrid ML/MAP estimator of $\boldsymbol{\eta}$ can be written as [53]

$$(\hat{\tau}, \hat{\nu}, \hat{\alpha}, \hat{\xi}) = \arg \max_{\tau, \nu, \alpha, \xi} f_{\mathbf{y}, \xi}(\mathbf{y}, \xi; \tau, \nu, \alpha), \quad (29)$$

where $f_{\mathbf{y}, \xi}(\mathbf{y}, \xi; \tau, \nu, \alpha)$ is the joint PDF of \mathbf{y} and ξ as a function of the deterministic parameters τ, ν and α

$$f_{\mathbf{y}, \xi}(\mathbf{y}, \xi; \tau, \nu, \alpha) = f_{\mathbf{y}|\xi}(\mathbf{y}|\xi; \tau, \nu, \alpha) f_{\xi}(\xi; \tau), \quad (30)$$

$f_{\mathbf{y}|\xi}(\mathbf{y}|\xi; \tau, \nu, \alpha)$ is the conditional PDF of \mathbf{y} given ξ , and $f_{\xi}(\xi; \tau)$ is the *a-priori* PDF of ξ . It follows from (20) and (26) that

$$f_{\mathbf{y}|\xi}(\mathbf{y}|\xi; \tau, \nu, \alpha) \quad (31)$$

$$= \frac{1}{(2\pi\sigma^2)^{NM}} \exp\left\{-\frac{\|\mathbf{y} - \alpha \Xi \mathbf{q}(\tau, \nu)\|^2}{2\sigma^2}\right\},$$

$$f_{\xi}(\xi; \tau) \quad (32)$$

$$= \frac{1}{\sqrt{(2\pi)^{NM} \det(\mathbf{R}(\tau))}} \exp\left\{-\frac{\xi^T \mathbf{R}(\tau)^{-1} \xi}{2}\right\}.$$

Plugging (30)–(32) into (29) yields

$$(\hat{\tau}, \hat{\nu}, \hat{\alpha}, \hat{\xi}) = \arg \min_{\tau, \nu, \alpha, \xi} \left\{ \frac{\|\mathbf{y} - \alpha \Xi \mathbf{q}(\tau, \nu)\|^2}{2\sigma^2} + \frac{\xi^T \mathbf{R}(\tau)^{-1} \xi + \log \det \mathbf{R}(\tau)}{2} \right\}. \quad (33)$$

For given τ, ν and ξ , the optimal estimate of α in (33) is given by

$$\hat{\alpha} = \frac{\mathbf{q}^H(\tau, \nu) \Xi^H \mathbf{y}}{\mathbf{q}^H(\tau, \nu) \Xi^H \Xi \mathbf{q}(\tau, \nu)} = \frac{\mathbf{q}^H(\tau, \nu) \Xi^H \mathbf{y}}{\|\mathbf{X}\|_F^2}, \quad (34)$$

where the last equality follows from (9), (10) and (28):

$$\|\mathbf{q}(\tau, \nu)\|^2 = \left\| \mathbf{F}_N^H \left(\mathbf{X} \odot \mathbf{b}(\tau) \mathbf{c}^H(\nu) \right) \right\|_F^2 = \|\mathbf{X} \odot \mathbf{b}(\tau) \mathbf{c}^H(\nu)\|_F^2 = \|\mathbf{X}\|_F^2. \quad (35)$$

Inserting (34) into (33), the hybrid ML/MAP problem becomes

$$(\hat{\tau}, \hat{\nu}, \hat{\xi}) = \arg \min_{\tau, \nu, \xi} \frac{\mathbf{y}^H \Pi_{\Xi \mathbf{q}(\tau, \nu)}^\perp \mathbf{y}}{\sigma^2} + \xi^T \mathbf{R}(\tau)^{-1} \xi + \log \det \mathbf{R}(\tau), \quad (36)$$

⁷Estimation of $\boldsymbol{\eta}$ should be performed for each new OFDM frame due to the time-varying nature of the PN and possible movement of the target in the delay-Doppler plane. Although the PN ξ has time-invariant statistics specified in (20), it will have a different (time-varying) realization in each frame and thus needs to be re-estimated by re-executing the proposed method in Sec. IV as new observations in the form of (26) arrive.

where

$$\begin{aligned}\mathbf{\Pi}_{\Xi\mathbf{q}(\tau,\nu)}^\perp &= \mathbf{I} - \frac{\Xi\mathbf{q}(\tau,\nu)\mathbf{q}^H(\tau,\nu)\Xi^H}{\|\mathbf{q}(\tau,\nu)\|^2} \\ &= \Xi\Xi^H - \frac{\Xi\mathbf{q}(\tau,\nu)\mathbf{q}^H(\tau,\nu)\Xi^H}{\|\mathbf{q}(\tau,\nu)\|^2} \\ &= \Xi \left(\mathbf{I} - \frac{\mathbf{q}(\tau,\nu)\mathbf{q}^H(\tau,\nu)}{\|\mathbf{q}(\tau,\nu)\|^2} \right) \Xi^H \\ &= \Xi\mathbf{\Pi}_{\mathbf{q}(\tau,\nu)}^\perp\Xi^H,\end{aligned}\quad (37)$$

with $\Xi\Xi^H = \mathbf{I}$ resulting from (27). Substituting (37) into (36), we obtain

$$(\hat{\tau}, \hat{\nu}, \hat{\xi}) = \arg \min_{\tau, \nu, \xi} \mathcal{L}(\tau, \nu, \xi), \quad (38)$$

where

$$\begin{aligned}\mathcal{L}(\tau, \nu, \xi) &= \frac{\mathbf{y}^H \Xi \mathbf{\Pi}_{\mathbf{q}(\tau,\nu)}^\perp \Xi^H \mathbf{y}}{\sigma^2} + \xi^T \mathbf{R}(\tau)^{-1} \xi \\ &\quad + \log \det \mathbf{R}(\tau).\end{aligned}\quad (39)$$

B. Iterated Small Angle Approximation

The hybrid ML/MAP optimization problem derived in (38) seems quite challenging to solve, primarily due to highly non-linear behavior of the high-dimensional PN vector ξ in the objective (39) (see (27)), leading to many local optima. A possible remedy to overcome such non-linearity is to employ *small angle approximation* (SAA) $e^{j\theta} \approx 1 + j\theta$ [29] for small θ . However, while this approach can work well for PN estimation in communications, it may lead to large errors in our sensing problem of interest. This is especially the case for distant targets since the PN variance increases with target delay, as seen from (18) and (19), invalidating the assumption of small θ .

To circumvent the non-linearity of PN in (39) and deal with large PN variances, we propose an *iterated small angle approximation* (ISAA) approach that invokes SAA around a given estimate of PN at each iteration, starting from an all-zeros estimate $\hat{\xi} = \mathbf{0}$. More specifically, suppose we have an estimate of PN vector at the i^{th} iteration, denoted by $\hat{\xi}^{(i)} \in \mathbb{R}^{NM \times 1}$, and we wish to approximate the exponential PN term $e^{-j\xi}$ in (39) around $\hat{\xi}^{(i)}$. To this end, we define the *residual PN*

$$\xi_\Delta = \xi - \hat{\xi}^{(i)} \quad (40)$$

for a given PN estimate $\hat{\xi}^{(i)}$. Re-writing (39) as a function of ξ_Δ , we have

$$\begin{aligned}\mathcal{L}(\tau, \nu, \xi_\Delta + \hat{\xi}^{(i)}) &= \frac{(\mathbf{v}^{(i)})^T \text{diag}(\mathbf{y})^H \mathbf{\Pi}_{\mathbf{q}(\tau,\nu)}^\perp \text{diag}(\mathbf{y}) (\mathbf{v}^{(i)})^*}{\sigma^2} \\ &\quad + (\xi_\Delta + \hat{\xi}^{(i)})^T \mathbf{R}(\tau)^{-1} (\xi_\Delta + \hat{\xi}^{(i)}) + \log \det \mathbf{R}(\tau),\end{aligned}\quad (41)$$

where $\mathbf{v}^{(i)} = e^{-j(\xi_\Delta + \hat{\xi}^{(i)})} \in \mathbb{C}^{NM \times 1}$. In order to solve (38) for ξ in an iterative fashion, we propose to solve the following minimization problem at the i^{th} iteration for the residual PN ξ_Δ , given a PN estimate $\hat{\xi}^{(i)}$ at hand:

$$(\hat{\tau}, \hat{\nu}, \hat{\xi}_\Delta) = \arg \min_{\tau, \nu, \xi_\Delta} \mathcal{L}(\tau, \nu, \xi_\Delta + \hat{\xi}^{(i)}). \quad (42)$$

To tackle (42), we invoke SAA for $\mathbf{v}^{(i)}$ in (41) around ξ_Δ to obtain

$$\mathbf{v}^{(i)} = e^{-j\hat{\xi}^{(i)}} \odot e^{-j\xi_\Delta} \approx e^{-j\hat{\xi}^{(i)}} \odot (\mathbf{1} - j\xi_\Delta). \quad (43)$$

Plugging (43) into the first term in (41), we obtain the approximation

$$\begin{aligned}(\mathbf{v}^{(i)})^T \text{diag}(\mathbf{y})^H \mathbf{\Pi}_{\mathbf{q}(\tau,\nu)}^\perp \text{diag}(\mathbf{y}) (\mathbf{v}^{(i)})^* &\approx \left[e^{-j\hat{\xi}^{(i)}} \odot (\mathbf{1} - j\xi_\Delta) \right]^T \text{diag}(\mathbf{y})^H \mathbf{\Pi}_{\mathbf{q}(\tau,\nu)}^\perp \text{diag}(\mathbf{y}) \\ &\quad \times \left[e^{j\hat{\xi}^{(i)}} \odot (\mathbf{1} + j\xi_\Delta) \right] \\ &= (\mathbf{1} - j\xi_\Delta)^T \mathbf{\Gamma}^{(i)}(\tau, \nu) (\mathbf{1} + j\xi_\Delta),\end{aligned}\quad (44)$$

where $\mathbf{\Gamma}^{(i)}(\tau, \nu) \in \mathbb{C}^{NM \times NM}$ is defined as⁸

$$\mathbf{\Gamma}^{(i)}(\tau, \nu) \triangleq \left[\text{diag}(\mathbf{y})^H \mathbf{\Pi}_{\mathbf{q}(\tau,\nu)}^\perp \text{diag}(\mathbf{y}) \right] \odot \left[e^{-j\hat{\xi}^{(i)}} (e^{j\hat{\xi}^{(i)}})^T \right]. \quad (45)$$

Now, substituting the approximation (44) into (41), we have

$$\mathcal{L}(\tau, \nu, \xi_\Delta + \hat{\xi}^{(i)}) \quad (46)$$

$$\approx \frac{1}{\sigma^2} (\mathbf{1} - j\xi_\Delta)^T \mathbf{\Gamma}^{(i)}(\tau, \nu) (\mathbf{1} + j\xi_\Delta) \quad (47)$$

$$\begin{aligned}&+ (\hat{\xi}^{(i)})^T \mathbf{R}(\tau)^{-1} \hat{\xi}^{(i)} + \xi_\Delta^T \mathbf{R}(\tau)^{-1} \xi_\Delta + 2\xi_\Delta^T \mathbf{R}(\tau)^{-1} \hat{\xi}^{(i)} \\ &+ \log \det \mathbf{R}(\tau)\end{aligned}\quad (48)$$

$$= \frac{1}{\sigma^2} \left[\mathbf{1}^T \Re \left\{ \mathbf{\Gamma}^{(i)}(\tau, \nu) \right\} \mathbf{1} + \xi_\Delta^T \Re \left\{ \mathbf{\Gamma}^{(i)}(\tau, \nu) \right\} \xi_\Delta \right] \quad (49)$$

$$\begin{aligned}&+ 2\xi_\Delta^T \Im \left\{ \mathbf{\Gamma}^{(i)}(\tau, \nu) \right\} \mathbf{1} + \xi_\Delta^T \mathbf{R}(\tau)^{-1} \xi_\Delta + 2\xi_\Delta^T \mathbf{R}(\tau)^{-1} \hat{\xi}^{(i)} \\ &+ (\hat{\xi}^{(i)})^T \mathbf{R}(\tau)^{-1} \hat{\xi}^{(i)} + \log \det \mathbf{R}(\tau)\end{aligned}$$

$$= \xi_\Delta^T \left(\frac{1}{\sigma^2} \Re \left\{ \mathbf{\Gamma}^{(i)}(\tau, \nu) \right\} + \mathbf{R}(\tau)^{-1} \right) \xi_\Delta \quad (49)$$

$$+ 2\xi_\Delta^T \left(\frac{1}{\sigma^2} \Im \left\{ \mathbf{\Gamma}^{(i)}(\tau, \nu) \right\} \mathbf{1} + \mathbf{R}(\tau)^{-1} \hat{\xi}^{(i)} \right)$$

$$+ \frac{1}{\sigma^2} \mathbf{1}^T \Re \left\{ \mathbf{\Gamma}^{(i)}(\tau, \nu) \right\} \mathbf{1} + (\hat{\xi}^{(i)})^T \mathbf{R}(\tau)^{-1} \hat{\xi}^{(i)} + \log \det \mathbf{R}(\tau),$$

where (48) is due to $\xi_\Delta^{(i)}$ being a real vector and $\mathbf{\Gamma}(\tau, \nu)$ being a Hermitian matrix (please see Appendix C for details).

Observing that (49) is quadratic in ξ_Δ , the optimal estimate of ξ_Δ that minimizes the approximated version of $\mathcal{L}(\tau, \nu, \xi_\Delta + \hat{\xi}^{(i)})$ in (49) can be written in closed-form for a given delay-Doppler pair (τ, ν) as follows:

$$\begin{aligned}\hat{\xi}_\Delta(\tau, \nu) &= -\mathbf{R}(\tau) \left(\Re \left\{ \mathbf{\Gamma}^{(i)}(\tau, \nu) \right\} \mathbf{R}(\tau) + \sigma^2 \mathbf{I} \right)^{-1} \\ &\quad \times \left(\Im \left\{ \mathbf{\Gamma}^{(i)}(\tau, \nu) \right\} \mathbf{1} + \sigma^2 \mathbf{R}(\tau)^{-1} \hat{\xi}^{(i)} \right).\end{aligned}\quad (50)$$

Finally, using the residual estimate in (50) and the definition in (40), the PN estimate can be updated as

$$\hat{\xi}^{(i+1)} = \hat{\xi}^{(i)} + \hat{\xi}_\Delta(\tau, \nu). \quad (51)$$

C. Alternating Optimization to Solve (38)

The iterative procedure developed in (50) and (51) for updating the PN estimate $\hat{\xi}$ as a function of delay and Doppler motivates an alternating optimization method to solve the original hybrid ML/MAP optimization problem (38). Hence, we propose to estimate delay, Doppler and PN in (38) using an *iterative refinement* approach that alternates between *PN estimation* and *delay-Doppler estimation* as follows:

- **Update $\hat{\xi}$ for Fixed (τ, ν) :** For a given delay-Doppler pair (τ, ν) , we compute the residual PN via (50) and update $\hat{\xi}$ via (51).

⁸Note that (44) is guaranteed to be real since $\mathbf{\Gamma}(\tau, \nu)$ in (45) is Hermitian.

Algorithm 1 Joint Delay, Doppler and PN Estimation with MAP Criterion via Iterated Small Angle Approximation (MAP-ISAA).

- 1: **Input:** Fast-time/slow-time observations \mathbf{Y} in (11), convergence thresholds ϵ_τ and ϵ_ν for delay and Doppler, and maximum number of iterations I_{\max} .
- 2: **Output:** Estimates of delay, Doppler and PN $\{\hat{\tau}, \hat{\nu}, \hat{\xi}\}$.
- 3: **Initialization:** Set $i = 0$.

- 1) Initialize the PN estimate to be the all-zeros vector, i.e., $\hat{\xi}^{(0)} = \mathbf{0}$, in accordance with (20).
- 2) Initialize the delay-Doppler pair to be the output of the standard 2-D FFT method, i.e.,

$$(\hat{\tau}^{(0)}, \hat{\nu}^{(0)}) = \arg \max_{\tau, \nu} \left| \mathbf{b}^H(\tau) (\mathbf{X}^* \odot \mathbf{F}_N \mathbf{Y}) \mathbf{c}(\nu) \right|^2.$$

4: **Iterated Approximation Steps:**

5: **while** $i < I_{\max}$

6: Update PN estimate via (50) and (51):

$$\hat{\xi}^{(i+1)} = \hat{\xi}^{(i)} + \hat{\xi}_\Delta(\hat{\tau}^{(i)}, \hat{\nu}^{(i)}).$$

7: Update delay-Doppler estimate via (53) and (54):

$$(\hat{\tau}^{(i+1)}, \hat{\nu}^{(i+1)}) = \arg \max_{\tau, \nu} \tilde{\mathcal{L}}(\tau, \nu, \hat{\xi}^{(i+1)}).$$

8: Set $i = i + 1$.

9: **if** $|\hat{\tau}^{(i)} - \hat{\tau}^{(i-1)}| \leq \epsilon_\tau$ and $|\hat{\nu}^{(i)} - \hat{\nu}^{(i-1)}| \leq \epsilon_\nu$

10: **break**

11: **end if**

12: **end while**

- **Update** (τ, ν) **for Fixed** $\hat{\xi}$: For a given PN estimate $\hat{\xi}$, we find the optimal delay-Doppler pair by solving (38):

$$(\hat{\tau}, \hat{\nu}) = \arg \min_{\tau, \nu} \mathcal{L}(\tau, \nu, \hat{\xi}), \quad (52)$$

which is equivalent to (please see Appendix D for details)

$$(\hat{\tau}, \hat{\nu}) = \arg \max_{\tau, \nu} \tilde{\mathcal{L}}(\tau, \nu, \hat{\xi}), \quad (53)$$

where

$$\tilde{\mathcal{L}}(\tau, \nu, \hat{\xi}) = \frac{\left| \mathbf{b}^H(\tau) \left[\mathbf{X}^* \odot \mathbf{F}_N (\widehat{\mathbf{W}}^* \odot \mathbf{Y}) \right] \mathbf{c}(\nu) \right|^2}{\sigma^2 \|\mathbf{X}\|_F^2} - \hat{\xi}^T \mathbf{R}(\tau)^{-1} \hat{\xi} - \log \det \mathbf{R}(\tau), \quad (54)$$

and $\widehat{\mathbf{W}} \triangleq \text{reshape}_{N,M} \left(e^{-j\hat{\xi}} \right)$.

The entire algorithm to solve (38) is summarized in Algorithm 1 and referred to as MAP-ISAA⁹. Under certain conditions, Algorithm 1 converges to a stationary point of (38) (please see Appendix E for a detailed convergence analysis). Employing the conjugate gradient (CG) method [29] to evaluate (50), the per-iteration complexity of Algorithm 1 can be obtained as (please see Appendix F for details)

$$\mathcal{O}(MN (\log M + (IM_0 + 1) \log N)), \quad (55)$$

where I is the number of CG iterations and M_0 is the number of dominant blocks of $\mathbf{R}(\tau)$ in (23), with $M_0 = 1$ for FROs due to Lemma 2 and $1 \leq M_0 \ll M$ for PLLs (typically, $M_0 \leq 3$).

⁹Algorithm 1 is agnostic to data symbols \mathbf{X} in the sense that it can work well with arbitrary \mathbf{X} and imposes no constraints on data symbols generated by the communications system.

V. EXTENSION TO RANGE-AMBIGUOUS TARGETS: FROM MITIGATION TO EXPLOITATION

We have up to now focused on how to estimate and *mitigate* PN in the OFDM sensing problem of interest. In this section, we extend the proposed estimation framework to the case of range-ambiguous targets and devise a PN *exploitation* approach to resolve range ambiguity.

A. PN Exploitation: Concept Description

An important peculiarity of PN in OFDM monostatic *sensing* is that it provides additional source of information on target delays that can be exploited to improve delay estimation performance, whereas PN in OFDM *communications* always degrades performance (e.g., [16], [19], [21], [46], [47]). More precisely, it is seen from (9), (20) and (28) that both $\mathbf{b}(\tau)$ and $\mathbf{R}(\tau)$, which are functions of the unknown delay τ , have an impact on the observation (26) and the hybrid ML/MAP cost function (39). Hence, in addition to the standard frequency-domain phase rotations in $\mathbf{b}(\tau)$, the covariance matrix $\mathbf{R}(\tau)$ of the PN vector conveys information on target delay. As noticed from the elements of $\mathbf{R}(\tau)$ in (17)–(21), there is no maximum unambiguous delay imposed by $\mathbf{R}(\tau)$ in estimating τ . This implies that we can detect the true ranges of the targets with $\tau > T$ by exploiting the information in $\mathbf{R}(\tau)$. However, for the ideal case without PN, we can only extract the delay information from $\mathbf{b}(\tau)$ (e.g., [12], [39], [40], [60]), which leads to range ambiguity for targets with $\tau > T$ due to the periodicity of the complex exponential terms in (9).

B. PN Exploitation: Proposed Algorithm

Let us consider a range-ambiguous target with true (unambiguous) delay $\tau = \tau_p + kT$ for some integer $k \geq 1$ denoting the ambiguity index, where $0 < \tau_p \leq T$ is the principal delay of the target, i.e., $\tau_p = \tau \pmod{T}$. Based on the observations in Sec. V-A, we propose to resolve the range ambiguity using the PN statistics represented by $\mathbf{R}(\tau)$. The key insight here is that the observation-related (first) term in (39) assumes the same value for τ and τ_p due to inherent range ambiguity in $\mathbf{b}(\cdot)$, while the statistics of the PN estimate $\hat{\xi}$ at the output of Algorithm 1 would match only with $\mathbf{R}(\tau)$ (not with $\mathbf{R}(\tau_p)$), enabling range ambiguity resolution¹⁰. Inspired by this insight, we formulate a parametric covariance matrix reconstruction problem¹¹ that minimizes the Frobenius distance between the sample matrix $\hat{\mathbf{R}} = \hat{\xi} \hat{\xi}^T$ and the parametric matrix $\mathbf{R}(\tau)$ in (23):

$$\hat{\tau}^{\text{true}} = \arg \min_{\tau} \|\mathbf{R}(\tau) - \hat{\mathbf{R}}\|_F^2, \quad (56)$$

potentially yielding the *unambiguous (true) delay estimate* $\hat{\tau}^{\text{true}}$. Exploiting the Toeplitz-block Toeplitz structure in (23), the problem (56) reduces to [67]

$$\hat{\tau}^{\text{true}} = \arg \min_{\tau} \left\| [\mathbf{R}(\tau)]_{0,:} - \hat{\mathbf{r}} \right\|^2, \quad (57)$$

where $[\mathbf{R}(\tau)]_{0,:}$ is the first row of $\mathbf{R}(\tau)$ and

$$\hat{\mathbf{r}}_i = \frac{1}{NM - i} \sum_{k=0}^{NM-i-1} \hat{\xi}_k \hat{\xi}_{k+i}, \quad (58)$$

with $\hat{\mathbf{r}} = [\hat{r}_0, \dots, \hat{r}_{NM-1}]^T$ and $\hat{\xi} = [\hat{\xi}_0, \dots, \hat{\xi}_{NM-1}]^T$.

¹⁰Please see Fig. 11(b) in Sec. VI-E for an illustration of this phenomenon.

¹¹The covariance matching problem formulated in (56) has a theoretical justification based on the extended invariance principle (EXIP) [65], [66] and the ML estimator of delay from $\hat{\xi}$. Please refer to Appendix G for details.

Algorithm 2 PN Exploitation to Resolve Range Ambiguity.

1: **Input:** Estimates of (ambiguous) delay and PN at the output of Algorithm 1 $\{\hat{\tau}, \hat{\xi}\}$.

2: **Output:** Unambiguous (true) estimate of delay $\hat{\tau}^{\text{true}}$.

- 1) Compute an estimate $\hat{\mathbf{r}} = [\hat{r}_0, \dots, \hat{r}_{NM-1}]^T$ of the first row of the PN covariance matrix $\mathbf{R}(\tau)$ in (23) by using the PN estimate $\hat{\xi}$:

$$\hat{r}_i = \frac{1}{NM-i} \sum_{k=0}^{NM-i-1} \hat{\xi}_k \hat{\xi}_{k+i}, \quad (59)$$

where $\hat{\xi} = [\hat{\xi}_0, \dots, \hat{\xi}_{NM-1}]^T$.

- 2) Construct the set of possible delay values by unfolding the ambiguous delay estimate $\hat{\tau}$ up to some maximum ambiguity index K :

$$\mathcal{T} = \{\tau \mid \tau = \hat{\tau} + kT, k = 0, \dots, K\}. \quad (60)$$

- 3) Find the unambiguous (true) estimate of delay by solving the parametric Toeplitz-block Toeplitz PN matrix reconstruction problem:

$$\hat{\tau}^{\text{true}} = \arg \min_{\tau \in \mathcal{T}} \|\mathbf{R}(\tau)_{0,:} - \hat{\mathbf{r}}\|^2. \quad (61)$$

In Algorithm 2, we present the proposed algorithm for range ambiguity resolution via PN exploitation. We restrict the search interval for range in Algorithm 1 such that the resulting delay estimate $\hat{\tau}$ is ambiguous. As seen from Algorithm 2, the prior information extracted from the PN estimates is exploited to find the range ambiguity index of the target (i.e., ambiguity resolution), while the principal range estimate of the target comes from Algorithm 1.

VI. SIMULATION RESULTS

In this section, we assess the performance of the proposed delay-Doppler estimation algorithm for PN-impaired OFDM radar sensing using the mmWave setting in Table I. In the observation model (11), the complex data symbols \mathbf{X} are chosen randomly from the QPSK constellation. To evaluate the RMSE performances, we generate a total of 2500 Monte Carlo realizations consisting of every combination of 50 independent realizations of PN vector ξ and AWGN vector \mathbf{z} in (26). Unless otherwise stated, we consider a target with $R = 30$ m and $v = 20$ m/s, and an oscillator with $f_{3\text{dB}} = 200$ kHz and $f_{\text{loop}} = 1$ MHz (in the case of PLL) [48]. Moreover, SNR is defined as $\text{SNR} = |\alpha|^2 / (2\sigma^2)$ according to the model in (11). To provide comparative performance analysis, we consider the following benchmark processing schemes:

- *MAP-ISAA*: The proposed hybrid ML/MAP estimation algorithm based on ISAA, described in Algorithm 1.
- *2-D FFT*: The standard 2-D FFT method used in OFDM radar processing [12], [39], [40], [60], [61], which corresponds to the optimal estimator in the ML sense in the absence of PN¹²:

$$(\hat{\tau}, \hat{\nu}) = \arg \max_{\tau, \nu} \left| \mathbf{b}^H(\tau) (\mathbf{X}^* \odot \mathbf{F}_N \mathbf{Y}) \mathbf{c}(\nu) \right|^2. \quad (62)$$

¹²The ML estimator in the absence of PN can be obtained as a special case of the hybrid ML/MAP estimator in (38) for known PN matrix with all elements being equal to 1, i.e., $\mathbf{W} = \mathbf{1}_{N \times M}$, as mentioned in Sec. II-D. This special case has already been derived in (52)–(54) for a given PN estimate $\hat{\mathbf{W}}$. Inserting $\hat{\mathbf{W}} = \mathbf{1}_{N \times M}$ and $\hat{\xi} = \mathbf{0}_{NM}$ into (54), one can readily derive the ML estimator in (62), which can be implemented via 2-D FFT as $\mathbf{b}(\tau)$ in (9) and $\mathbf{c}(\nu)$ in (10) are DFT matrix columns for a uniformly sampled delay-Doppler grid.

TABLE I
OFDM SIMULATION PARAMETERS

Parameter	Value
Carrier Frequency, f_c	28 GHz
Total Bandwidth, B	50 MHz
Number of Subcarriers, N	256
Number of Symbols, M	10
Subcarrier Spacing, Δf	195.31 kHz
Symbol Duration, T	5.12 μs
Cyclic Prefix Duration, T_{cp}	1.28 μs
Total Symbol Duration, T_{sym}	6.40 μs

- *2-D FFT (PN-free)*: The 2-D FFT method applied on the PN-free version of the radar observations, $\mathbf{Y}^{\text{PN-free}}$, in (12):

$$(\hat{\tau}, \hat{\nu}) = \arg \max_{\tau, \nu} \left| \mathbf{b}^H(\tau) (\mathbf{X}^* \odot \mathbf{F}_N \mathbf{Y}^{\text{PN-free}}) \mathbf{c}(\nu) \right|^2. \quad (63)$$

This benchmark will provide insights into PN-induced performance losses and gains in delay-Doppler estimation.

Besides the above schemes, we also plot the hybrid CRBs [52], [53] to quantify the theoretical performance bounds. The hybrid CRB in the presence and absence of PN will be denoted as “CRB” and “CRB (PN-free)”, respectively, which theoretically lower-bound the RMSE of “MAP-ISAA” and “2-D FFT (PN-free)” algorithms.

In what follows, we first evaluate the RMSE performances of the considered processing schemes under various operating conditions with regard to SNR, oscillator quality and target range. Then, we illustrate the convergence behavior of the proposed algorithm in Algorithm 1. Finally, we demonstrate the PN exploitation capability of the proposed approach in Algorithm 2.

A. Performance with respect to SNR

We first assess the performance of the proposed MAP-ISAA algorithm, along with the FFT-based benchmark methods, with respect to SNR. Fig. 3 and Fig. 4 show (for FRO and PLL architectures, respectively) the range and velocity RMSEs of the considered schemes¹³. In terms of ranging performance in Fig. 3(a) and Fig. 4(a), the proposed algorithm achieves the CRB and significantly outperforms the 2-D FFT benchmark for both FRO and PLL architectures, especially at medium and high SNRs, where an order-of-magnitude improvement in ranging accuracy can be observed. It is seen that the performance of the standard FFT method saturates above a certain SNR level, while the proposed approach can effectively utilize the prior information on PN to compensate for its impact on the observations and avoid such saturation behavior by attaining its theoretical lower bound (which decreases with increasing SNR). Moreover, in compliance with the theoretical bounds, MAP-ISAA exhibits ranging performance very close to that achieved in the absence of PN, which evidences its remarkable PN compensation capability.

In contrast to their ranging performances, FRO and PLL display different trends in velocity estimation, depicted in Fig. 3(b) and Fig. 4(b). For PLL, the MAP-ISAA algorithm can provide noticeable improvements in velocity RMSE over the FFT benchmark, leading to gains on the order of several 10 cm/s, while in case of FRO performance gains seem negligible with respect to the FFT method. The same observation

¹³Due to discretization of search space and its confinement to a finite interval for practical implementation of the estimators, the RMSE might slightly fall below the CRB in certain rare scenarios.

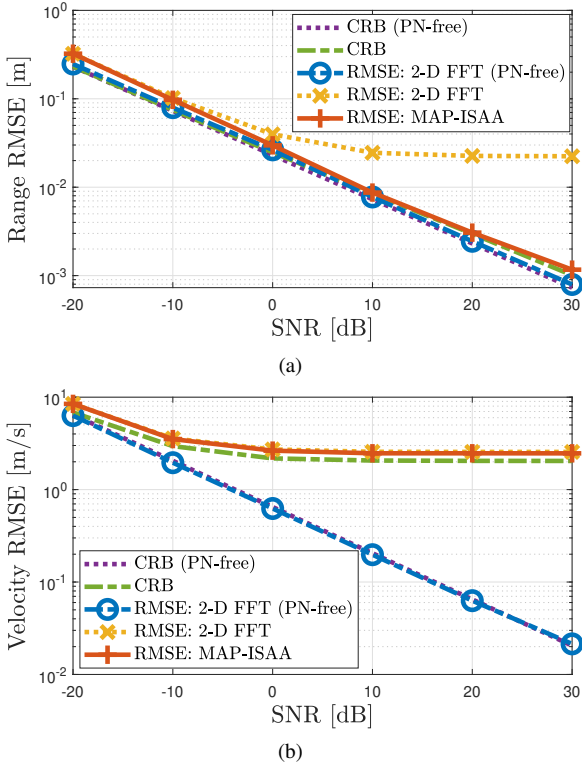


Fig. 3. (a) Range and (b) velocity RMSE with respect to SNR for FRO with $f_{3dB} = 200$ kHz.

is also valid when comparing the CRB to the RMSE of the FFT method since MAP-ISAA can get very close to the CRB for both types of oscillators. This difference between FRO and PLL in velocity estimation can be attributed to the following two facts: (i) velocity information in (11) is extracted from *slow-time* (symbol-to-symbol) phase rotations represented by $c(\nu)$ in (10), and (ii) PN samples in different symbols are *uncorrelated* for FRO, while they can be *correlated* for PLL, as shown in (23), Lemma 2 and Fig. 2. Therefore, correlation of PN across symbols can be exploited in PLL for accurate PN estimation and compensation in slow-time, leading to better velocity estimates compared to FRO. In this respect, similar ranging performances for FRO and PLL can be explained by pointing out high correlation of PN in *fast-time* for both oscillator types, represented by the block-diagonals $\mathbf{R}_0(\tau)$ in (23) and (25).

Comparing the asymptotic trends of the MAP-ISAA algorithm, as well as the corresponding CRB, between range and velocity estimation in Fig. 3 and Fig. 4, we observe plateau in velocity estimation performance as opposed to monotonically decreasing errors for range estimation. In connection with this, PN causes only slight degradation of ranging performance, whereas velocity estimation can be severely degraded by PN. This is due to the fact that range information is gathered from frequency-domain (or, equivalently, fast-time) phase shifts across $\mathbf{b}(\tau)$ in (9), while velocity information comes from slow-time phase shifts in (10). Since PN enjoys much higher correlation in fast-time than in slow-time, such correlation can be utilized to cancel out its effect in fast-time and accordingly provide accurate range estimates.

B. Performance with respect to Oscillator Quality

We now investigate the performance of the considered schemes with respect to oscillator quality for both FRO and PLL implementations. To this end, in Fig. 5 we report

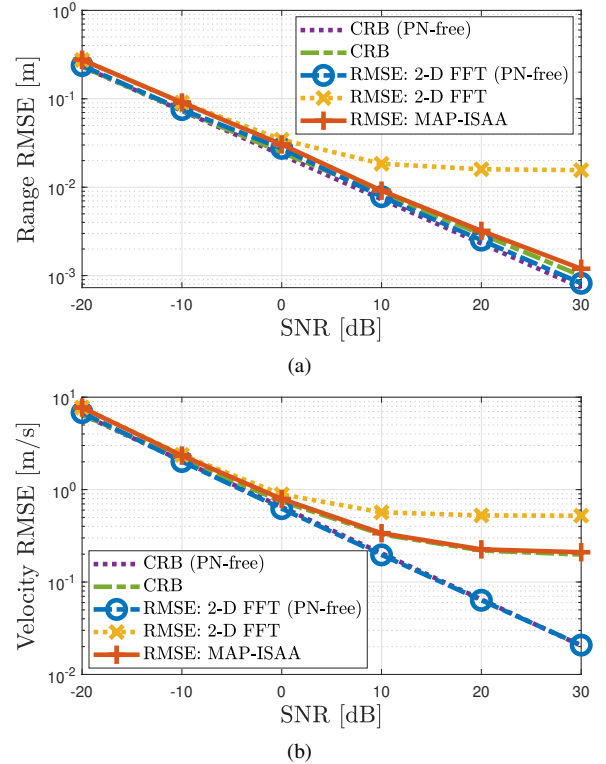


Fig. 4. (a) Range and (b) velocity RMSE with respect to SNR for PLL with $f_{3dB} = 200$ kHz and $f_{loop} = 1$ MHz.

accuracy in range, velocity and PN estimation¹⁴ against the 3 dB bandwidth f_{3dB} of FRO at SNR = 20 dB. It can be observed that the ranging performance of the proposed MAP-ISAA algorithm is highly robust in the face of worsening oscillator quality (i.e., increasing f_{3dB}), maintaining almost the same RMSE level and attaining the corresponding bounds over a wide range of f_{3dB} values. On the other hand, the FFT benchmark suffers from a considerable performance degradation as f_{3dB} increases due to increasing PN variance, shown in Fig. 5(c). Additionally, range accuracy obtained by MAP-ISAA is very close to that achievable in the absence of PN for all f_{3dB} values, which demonstrates the effectiveness of the proposed PN estimation/compensation approach in Algorithm 1. Regarding velocity RMSE, similar trends to those in Sec. VI-A can be observed for both the CRB and the RMSE of MAP-ISAA, due to lack of PN correlation in slow-time (i.e., the block-diagonal structure of PN covariance matrix for FRO, as specified in Lemma 2).

Next, we consider the RMSE performances for PLL synthesizers in Fig. 6, which shows accuracies against the PLL loop bandwidth f_{loop} . In terms of both range and velocity RMSEs, the PN-ignorant FFT method performs worse with decreasing f_{loop} since PN variance increases as f_{loop} decreases, as seen from (19) and Fig. 6(c). On the other hand, the proposed algorithm attains the same ranging accuracy for the entire interval of f_{loop} values from 10 kHz to 10 MHz, proving its robustness against the quality of PLL synthesizer. Hence, the performance gain of MAP-ISAA in range estimation with respect to the FFT benchmark becomes more pronounced with decreasing PLL quality (i.e., decreasing f_{loop}). Moreover, the ranging performance of the proposed approach under the impact of PN is near that of the FFT benchmark that uses

¹⁴The PN RMSE is defined as $[\sum_{c=1}^C \|\hat{\xi}_c - \xi_c\|^2 / (NMC)]^{1/2}$, where $\hat{\xi}_c \in \mathbb{R}^{NM \times 1}$ and $\xi_c \in \mathbb{R}^{NM \times 1}$ denote, respectively, the estimated and true PN at the c^{th} Monte Carlo realization and $C = 2500$. For the 2-D FFT method, we set $\hat{\xi}_c = \mathbf{0}$.

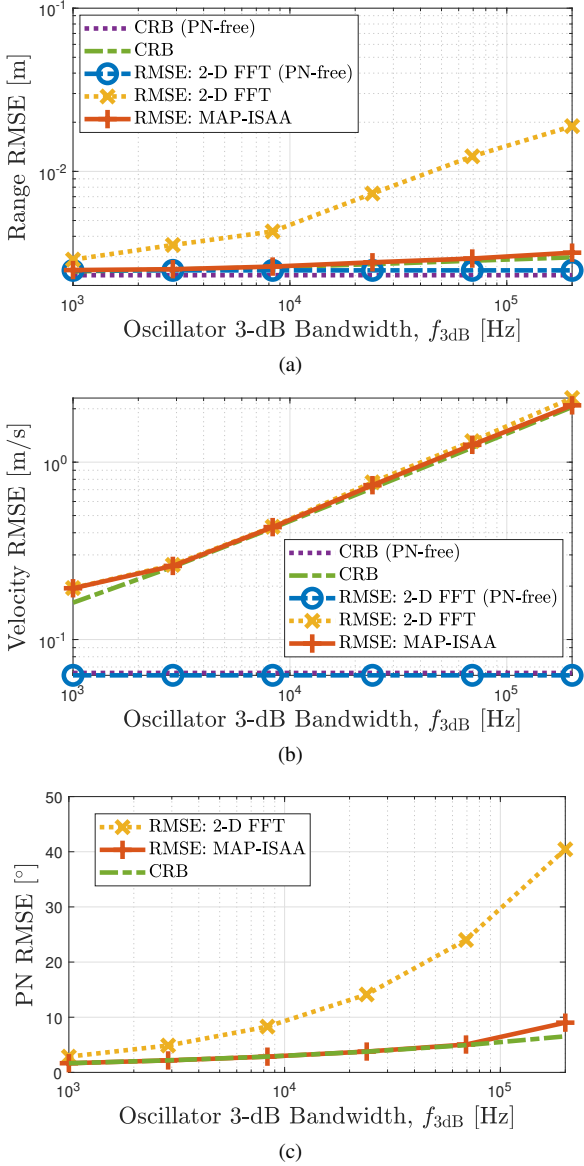


Fig. 5. (a) Range, (b) velocity and (c) PN RMSE with respect to 3 dB bandwidth f_{3dB} of FRO at SNR = 20 dB.

PN-free radar observations over a broad range of f_{loop} values, which indicates almost perfect cancellation of the effect of PN. Furthermore, the velocity RMSE curves in Fig. 6(b) reveal that MAP-ISAA performs very close to CRB and can provide gains on the order of 10 cm/s over the FFT benchmark. Finally, from Fig. 5 and Fig. 6, we note that MAP-ISAA can achieve the CRBs on range, velocity and PN estimation for both FROs and PLLs under various levels of oscillator quality.

C. Performance with respect to Target Range

To further highlight the benefits of the proposed algorithm, we explore the impact of target range on the performance of the processing schemes under consideration, recalling the delay-dependent statistics of PN derived in Sec. III. In Fig. 7 and Fig. 8, we show the range-velocity RMSEs versus target range for FRO and PLL, respectively. As can be noticed, the ranging performance of the proposed approach is robust against increasing target range for both FRO and PLL implementations, which suggest that Algorithm 1 can successfully utilize the knowledge of delay-dependent PN covariance $\mathbf{R}(\tau)$ to jointly estimate the coupled delay and PN parameters. However, the FFT method experiences substantial loss in ranging accuracy as target moves further away from radar, in

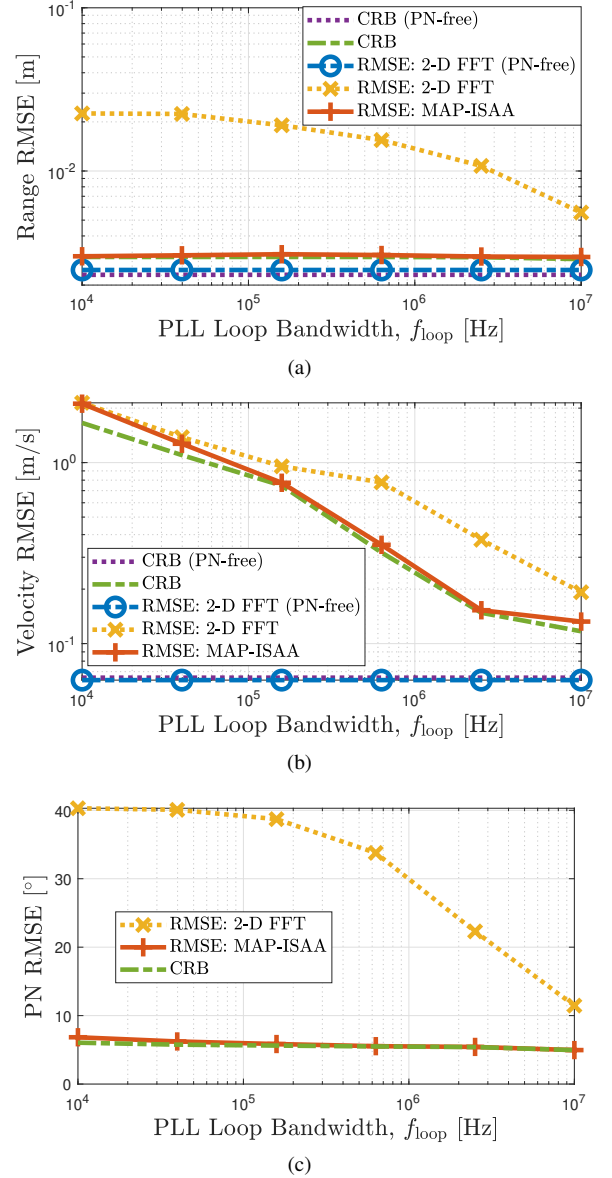


Fig. 6. (a) Range, (b) velocity and (c) PN RMSE with respect to loop bandwidth f_{loop} of PLL with $f_{3dB} = 200$ kHz at SNR = 20 dB.

compliance with monotonically increasing variance of PN as a function of delay in (18) and (19). Moreover, comparing MAP-ISAA and CRB against the PN-free benchmark, PN-induced performance degradation is only marginal, which agrees with the observations in Sec. VI-A and Sec. VI-B. Furthermore, looking at the velocity RMSEs in Fig. 7(b) and Fig. 8(b), we observe that improvements on the order of m/s can be provided by the proposed algorithm over the FFT benchmark for PLL, whereas no noticeable gains occur in case of FRO. This further corroborates the above-mentioned insights on the impact of different PN correlation characteristics of FRO and PLL (specified in (23) and (25)) onto velocity accuracy.

D. Convergence Behavior of the Proposed Algorithm

To illustrate the convergence behavior of the proposed MAP-ISAA algorithm in Algorithm 1 through iterated approximations, Fig. 9 demonstrates the evolution of range, velocity and PN RMSEs over consecutive iterations for PLL. It is observed that starting from the output of the FFT benchmark, Algorithm 1 monotonically converges to the corresponding CRBs on range, velocity and PN estimation within few iterations, which proves the effectiveness of the proposed iterated SAA approach. To explore the effect of iterated approximations on

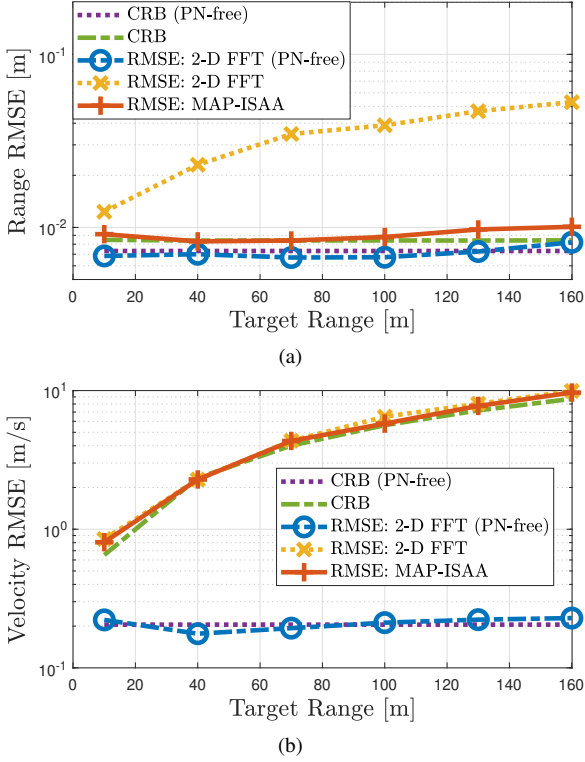


Fig. 7. (a) Range, and (b) velocity RMSE with respect to target range for FRO with $f_{3\text{dB}} = 150$ kHz at SNR = 10 dB.

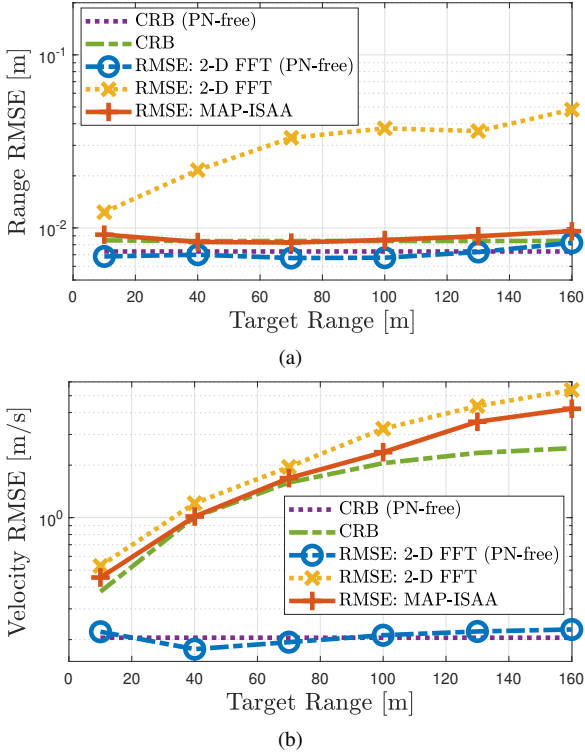


Fig. 8. (a) Range, and (b) velocity RMSE with respect to target range for PLL with $f_{3\text{dB}} = 150$ kHz and $f_{1\text{oop}} = 100$ kHz at SNR = 10 dB.

PN tracking performance, in Fig. 10 we depict instances from the PN process along with the PN estimates at the first and last iteration of Algorithm 1 for FRO and PLL architectures¹⁵. Comparing the results of the first and last iterations, we see that by applying iterated approximations in Algorithm 1, PN tracking accuracy significantly improves around regions with high fluctuations, which verifies the superiority of the proposed

¹⁵Phase wrapping in PN trajectories (i.e., phases outside $[-\pi, \pi]$) occurs very rarely and does not affect the resulting RMSE performances.

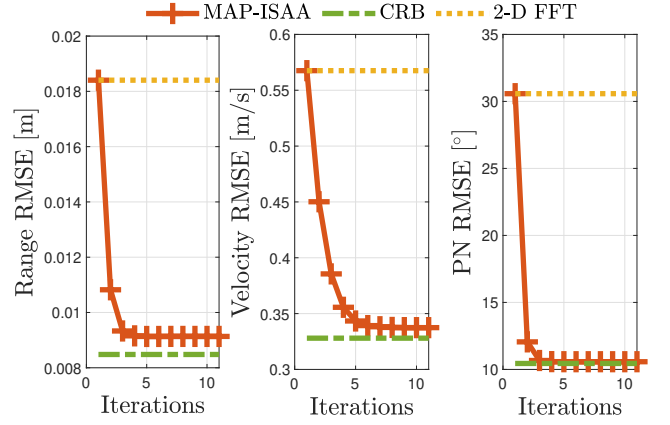


Fig. 9. Evolution of range, velocity and PN RMSEs through successive iterations of the proposed algorithm at SNR = 10 dB for PLL with $f_{3\text{dB}} = 200$ kHz and $f_{1\text{oop}} = 1$ MHz. Initialized at the FFT output, the proposed approach can quickly converge to the corresponding CRBs in few iterations, recovering the performance loss incurred by the PN.

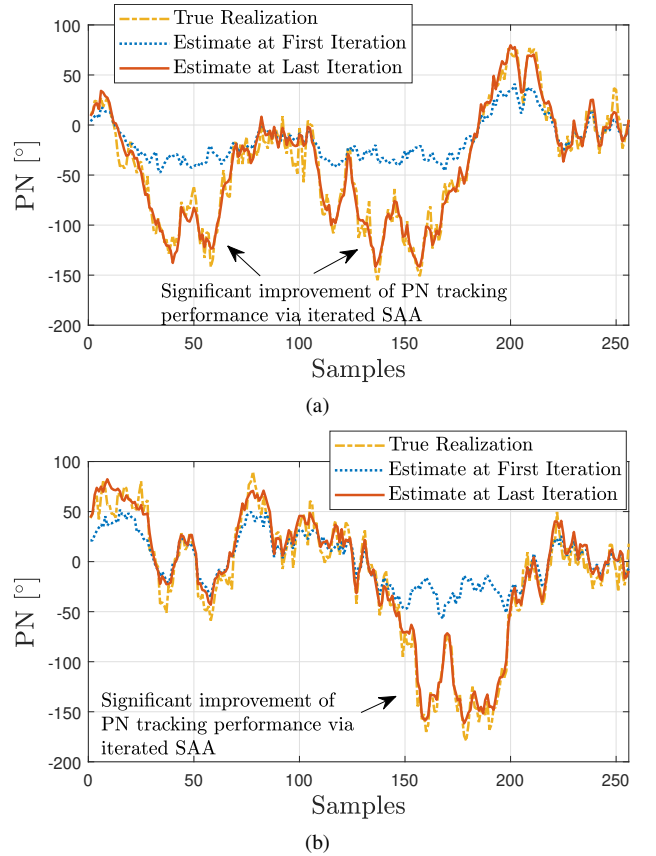


Fig. 10. True PN realization and PN estimates at the first and last iteration of the proposed algorithm at SNR = 10 dB for (a) FRO with $f_{3\text{dB}} = 150$ kHz considering a target with range $R = 100$ m, and (b) PLL with $f_{3\text{dB}} = 150$ kHz and $f_{1\text{oop}} = 100$ kHz considering a target with range $R = 130$ m. The proposed iterated SAA approach provides substantial improvements in PN trajectory tracking performance especially when large fluctuations occur.

iterative refinement approach.

E. PN Exploitation Capability of the Proposed Algorithm

In this part, we demonstrate the PN exploitation capability of the proposed method in Algorithm 2 by considering a target located at $R = 1000$ m, which is beyond the maximum unambiguous range of 768 m according to Table I. In Fig. 11(a), we plot the range RMSE vs. SNR for PLL with $f_{3\text{dB}} = 20$ kHz and $f_{1\text{oop}} = 1$ MHz by searching for the first two ambiguity intervals in (60), i.e., $K = 1$. In addition, Fig. 11(b) shows the PN covariances at SNR = 20 dB, obtained via the estimate $\hat{\mathbf{r}}$ in (59) and via the analytical evaluation $[\mathbf{R}(\tau)]_0$ in (61) at the

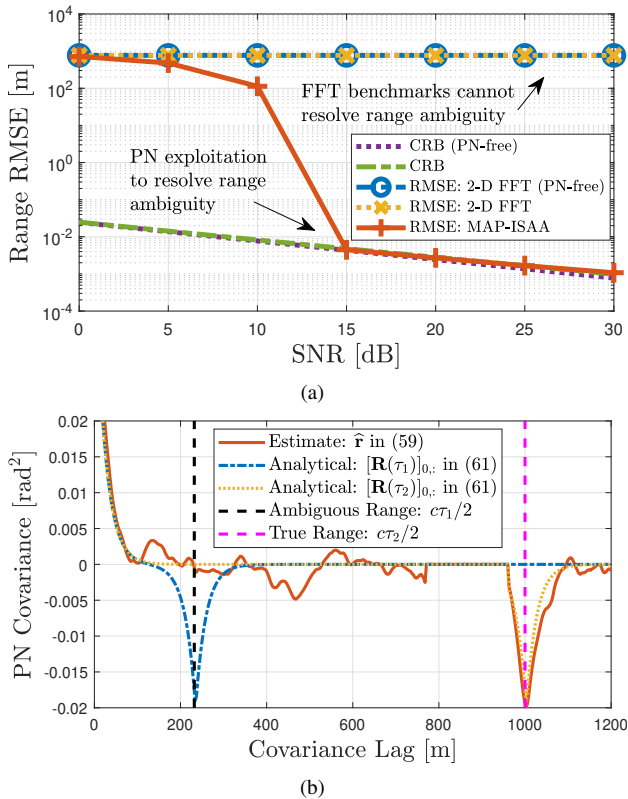


Fig. 11. PN exploitation to resolve range ambiguity for PLL with $f_{3\text{dB}} = 20$ kHz and $f_{\text{loop}} = 1$ MHz, where target is located at $R = 1000$ m. (a) Range RMSE with respect to SNR. (b) PN covariance at SNR = 20 dB, corresponding to the estimate $\hat{\mathbf{r}}$ in (59) and the analytical expression $[\mathbf{R}(\tau)]_{0,\cdot}$ in (61) evaluated at $\tau_1 = \hat{\tau}$ and $\tau_2 = \hat{\tau} + T$, where $\hat{\tau}$ is the ambiguous delay estimate. The proposed approach in Algorithm 2 can correctly identify the true target range by exploiting PN statistics ($\hat{\mathbf{r}}$ matches with $[\mathbf{R}(\tau_2)]_{0,\cdot}$), while the FFT benchmark fails to resolve range ambiguity irrespective of whether the PN is present or absent.

ambiguous and true ranges. It can be seen that the proposed PN exploitation approach can successfully resolve the range ambiguity starting from SNR = 15 dB (when the PN estimate becomes sufficiently accurate¹⁶) and attain the corresponding CRB, whereas neither of the FFT benchmarks can correctly identify the true target range due to intrinsic range ambiguity in $\mathbf{b}(\tau)$, in compliance with the discussions in Sec. V. More specifically, the FFT processing in (62), either using PN-impaired observations \mathbf{Y} in (11) or PN-free observations $\mathbf{Y}^{\text{PN-free}}$ in (12), can extract the range information only from $\mathbf{b}(\tau)$, which causes ambiguity for $\tau > T$ (see (9)). On the other hand, to estimate the true (unambiguous) range of the target, Algorithm 2 can effectively exploit the ranging information revealed by the PN statistics $\mathbf{R}(\tau)$ in (20), which does not introduce any ambiguity in estimating τ as noticed from (17)–(21). Surprisingly, the proposed approach under the impact of PN can significantly outperform the FFT benchmark that uses ideal, PN-free observations, indicating its excellent PN exploitation performance.

VII. CONCLUDING REMARKS

In this work, we have investigated the problem of monostatic radar sensing in OFDM JRC systems under the effect of PN. Starting from an explicit derivation of PN statistics in the

¹⁶Additional simulations with different $f_{3\text{dB}}$ values for PLL offer an intriguing insight into the relation between $f_{3\text{dB}}$ and the degree of accuracy improvement via PN exploitation: higher $f_{3\text{dB}}$ (which means lower oscillator quality) provides improved resolvability of range ambiguity at low SNRs through more pronounced notches in the PN covariance profile at the ambiguous and true ranges, while leading to lower accuracy at high SNRs due to performance saturation (i.e., when the ambiguity is already resolved).

OFDM radar receiver, we have proposed a novel algorithm for joint estimation of delay, Doppler and PN by devising an iterated small angle approximation approach that solves the hybrid ML/MAP optimization problem through alternating updates of delay-Doppler and PN estimates. In addition, we have developed a PN exploitation algorithm that uses the statistics of the PN estimates to resolve range ambiguity. To assess the performance of the proposed algorithms, comprehensive simulations have been carried out over a broad range of operating conditions, leading to the following key findings:

- *Range vs. Velocity Accuracy under PN*: The proposed MAP-ISAA algorithm significantly outperforms the FFT benchmark in ranging accuracy, while providing slight improvements in velocity accuracy. This results from strong (weak) correlation of PN in fast-time (slow-time).
- *Impact of Oscillator Type - FRO vs. PLL*: FROs and PLLs lead to very similar performance in range estimation, whereas PLLs can provide much higher velocity accuracy than FROs. This is due to the absence of PN correlation in slow-time for FROs.
- *Scenarios with Significant Impact of PN on Sensing*: The effect of PN on sensing performance becomes more significant at higher SNRs, for oscillators with larger $f_{3\text{dB}}$ and smaller f_{loop} values, and farther targets. In such scenarios, PN should be considered in algorithm design.
- *Iterated Small Angle Approximation*: The proposed algorithm enjoys fast convergence to the hybrid CRB and provides superior PN tracking performance via iterated approximations.
- *PN Exploitation*: Delay-dependency of PN statistics can be effectively exploited to resolve range ambiguity above a certain SNR level, thereby converting the detrimental effect of PN into something beneficial for radar sensing.

As future research, we plan to investigate extensions of the proposed framework to MIMO architectures and the multi-target case.

APPENDIX A

CORRELATION FUNCTION OF DIFFERENTIAL PHASE NOISE IN (17)

Let the correlation function of $\phi(t)$ in (14) be defined as

$$R_{\phi\phi}(t_1, t_2) \triangleq \mathbb{E}[\phi(t_1)\phi(t_2)] . \quad (64)$$

Then, it follows from (15) that

$$\mathbb{E}[\xi(t_1, \tau)\xi(t_2, \tau)] = R_{\phi\phi}(t_1, t_2) - R_{\phi\phi}(t_1, t_2 - \tau) - R_{\phi\phi}(t_1 - \tau, t_2) + R_{\phi\phi}(t_1 - \tau, t_2 - \tau) . \quad (65)$$

From (15) and (16), we have

$$\sigma_{\xi}^2(\tau) = \mathbb{E}[\xi(t, \tau)^2] = \sigma_{\phi}^2(t) + \sigma_{\phi}^2(t - \tau) - 2R_{\phi\phi}(t, t - \tau) , \quad (66)$$

which yields

$$R_{\phi\phi}(t_1, t_2) = \frac{\sigma_{\phi}^2(t_1) + \sigma_{\phi}^2(t_2) - \sigma_{\xi}^2(t_1 - t_2)}{2} . \quad (67)$$

Finally, inserting (67) into (65) yields

$$\begin{aligned} \mathbb{E}[\xi(t_1, \tau)\xi(t_2, \tau)] & \\ &= \frac{\sigma_{\xi}^2(t_1 - t_2 + \tau) + \sigma_{\xi}^2(t_1 - t_2 - \tau)}{2} - \sigma_{\xi}^2(t_1 - t_2) . \end{aligned} \quad (68)$$

Defining $\Delta t \triangleq t_1 - t_2$ in (68) and considering $\sigma_{\xi}^2(\tau) = \sigma_{\xi}^2(-\tau)$, we obtain the result in (17).

APPENDIX B

BLOCK-DIAGONAL STRUCTURE OF $\mathbf{R}(\tau)$ FOR FROS

Using (18) in (17), we obtain the correlation function for FROS as

$$R_{\xi\xi}(\Delta t, \tau) = 4\pi f_{3\text{dB}} \max(\tau - |\Delta t|, 0). \quad (69)$$

Since $|\Delta t_{n_1 n_2}^{(m)}| \geq T_{\text{cp}}$ for $m > 0$ in (24), we have $R_{\xi\xi}(\Delta t_{n_1 n_2}^{(m)}, \tau) = 0$ for $m > 0$ and $\tau \leq T_{\text{cp}}$ from (69), leading to $\mathbf{R}_m(\tau) = \mathbf{0}$ for $m > 0$, which yields (25).

APPENDIX C

OBTAINING (48) FROM (47)

In this part, we provide details on how to reach (48) from (47). To this end, we present the following auxiliary lemmas.

Lemma 3. For any $\mathbf{x} \in \mathbb{R}^{N \times 1}$ and any Hermitian matrix $\mathbf{A} \in \mathbb{C}^{N \times N}$, the following equality holds:

$$\mathbf{x}^T \mathbf{A} \mathbf{x} = \mathbf{x}^T \Re\{\mathbf{A}\} \mathbf{x}. \quad (70)$$

Proof. Since $\mathbf{x}^T \mathbf{A} \mathbf{x}$ is scalar, we can write

$$\mathbf{x}^T \mathbf{A} \mathbf{x} = (\mathbf{x}^T \mathbf{A} \mathbf{x})^T = \mathbf{x}^T \mathbf{A}^T \mathbf{x} \stackrel{(a)}{=} \mathbf{x}^T \mathbf{A}^* \mathbf{x}, \quad (71)$$

where (a) is due to \mathbf{A} being Hermitian, i.e., $\mathbf{A}^H = \mathbf{A}$. Rewriting the leftmost and rightmost terms in (71), we obtain

$$\begin{aligned} \mathbf{x}^T \mathbf{A} \mathbf{x} &= \mathbf{x}^T (\Re\{\mathbf{A}\} + j\Im\{\mathbf{A}\}) \mathbf{x} \\ &= \mathbf{x}^T \mathbf{A}^* \mathbf{x} = \mathbf{x}^T (\Re\{\mathbf{A}\} - j\Im\{\mathbf{A}\}) \mathbf{x}, \end{aligned} \quad (72)$$

which leads to

$$\mathbf{x}^T \Im\{\mathbf{A}\} \mathbf{x} = 0. \quad (73)$$

Substituting (73) into (72) yields the result in (74). ■

Lemma 4. For any $\mathbf{x} \in \mathbb{R}^{N \times 1}$, $\mathbf{y} \in \mathbb{R}^{N \times 1}$ and any Hermitian matrix $\mathbf{A} \in \mathbb{C}^{N \times N}$, the following equality holds:

$$j(\mathbf{x}^T \mathbf{A} \mathbf{y} - \mathbf{y}^T \mathbf{A} \mathbf{x}) = 2\mathbf{y}^T \Im\{\mathbf{A}\} \mathbf{x}. \quad (74)$$

Proof. Since $\mathbf{x}^T \mathbf{A} \mathbf{y}$ is scalar and \mathbf{A} is Hermitian, we can write

$$\begin{aligned} j(\mathbf{x}^T \mathbf{A} \mathbf{y} - \mathbf{y}^T \mathbf{A} \mathbf{x}) &= j(\mathbf{y}^T \mathbf{A}^T \mathbf{x} - \mathbf{y}^T \mathbf{A} \mathbf{x}) \\ &= j(\mathbf{y}^T \mathbf{A}^* \mathbf{x} - \mathbf{y}^T \mathbf{A} \mathbf{x}) \\ &= j\mathbf{y}^T (\mathbf{A}^* - \mathbf{A}) \mathbf{x} \\ &= -j\mathbf{y}^T 2j\Im\{\mathbf{A}\} \mathbf{x} \\ &= 2\mathbf{y}^T \Im\{\mathbf{A}\} \mathbf{x}, \end{aligned}$$

which completes the proof. ■

Opening up the first term in (47), we have

$$(\mathbf{1} - j\xi_\Delta)^T \mathbf{\Gamma}^{(i)}(\tau, \nu) (\mathbf{1} + j\xi_\Delta) \quad (75)$$

$$= \mathbf{1}^T \mathbf{\Gamma}^{(i)}(\tau, \nu) \mathbf{1} + \xi_\Delta^T \mathbf{\Gamma}^{(i)}(\tau, \nu) \xi_\Delta \quad (76)$$

$$\begin{aligned} &+ j \left(\mathbf{1}^T \mathbf{\Gamma}^{(i)}(\tau, \nu) \xi_\Delta - \xi_\Delta^T \mathbf{\Gamma}^{(i)}(\tau, \nu) \mathbf{1} \right) \\ &= \mathbf{1}^T \Re\left\{ \mathbf{\Gamma}^{(i)}(\tau, \nu) \right\} \mathbf{1} + \xi_\Delta^T \Re\left\{ \mathbf{\Gamma}^{(i)}(\tau, \nu) \right\} \xi_\Delta \\ &+ 2\xi_\Delta^T \Im\left\{ \mathbf{\Gamma}(\tau, \nu) \right\} \mathbf{1}, \end{aligned} \quad (77)$$

where the transition from (76) to (77) is via Lemma 3 and Lemma 4. Plugging (75)–(77) into (47) yields (48).

APPENDIX D

DELAY-DOPPLER ESTIMATION IN (52)

Using (27), (35) and (39) in (52), we obtain

$$\begin{aligned} \mathcal{L}(\tau, \nu, \hat{\xi}) &= \frac{1}{\sigma^2} \left(e^{j\hat{\xi}} \odot \mathbf{y} \right)^H \mathbf{\Pi}_{\mathbf{q}(\tau, \nu)}^\perp \left(e^{j\hat{\xi}} \odot \mathbf{y} \right) + \hat{\xi}^T \mathbf{R}(\tau)^{-1} \hat{\xi} \\ &+ \log \det \mathbf{R}(\tau) \\ &= \frac{1}{\sigma^2} \left(e^{j\hat{\xi}} \odot \mathbf{y} \right)^H \left(\mathbf{I} - \frac{\mathbf{q}(\tau, \nu) \mathbf{q}^H(\tau, \nu)}{\|\mathbf{X}\|_F^2} \right) \left(e^{j\hat{\xi}} \odot \mathbf{y} \right) \\ &+ \hat{\xi}^T \mathbf{R}(\tau)^{-1} \hat{\xi} + \log \det \mathbf{R}(\tau) \\ &= \frac{\|\mathbf{y}\|^2}{\sigma^2} - \frac{\left| \mathbf{q}^H(\tau, \nu) \left(e^{j\hat{\xi}} \odot \mathbf{y} \right) \right|^2}{\sigma^2 \|\mathbf{X}\|_F^2} + \hat{\xi}^T \mathbf{R}(\tau)^{-1} \hat{\xi} \\ &+ \log \det \mathbf{R}(\tau). \end{aligned} \quad (78)$$

Based on (78), the problem (52) is equivalent to

$$\begin{aligned} (\hat{\tau}, \hat{\nu}) &= \arg \max_{\tau, \nu} \frac{\left| \mathbf{q}^H(\tau, \nu) \left(e^{j\hat{\xi}} \odot \mathbf{y} \right) \right|^2}{\sigma^2 \|\mathbf{X}\|_F^2} - \hat{\xi}^T \mathbf{R}(\tau)^{-1} \hat{\xi} \\ &- \log \det \mathbf{R}(\tau). \end{aligned} \quad (79)$$

Using (28) in the first term of (79) and defining $\widehat{\mathbf{W}} \triangleq \text{reshape}_{N, M} \left(e^{-j\hat{\xi}} \right)$, we have

$$\begin{aligned} &\left| \mathbf{q}^H(\tau, \nu) \left(e^{j\hat{\xi}} \odot \mathbf{y} \right) \right|^2 \\ &= \left| \text{tr} \left(\left[\mathbf{F}_N^H (\mathbf{X} \odot \mathbf{b}(\tau) \mathbf{c}^H(\nu)) \right]^H \left[\widehat{\mathbf{W}}^* \odot \mathbf{Y} \right] \right) \right|^2 \\ &= \left| \text{tr} \left(\left(\mathbf{X} \odot \mathbf{b}(\tau) \mathbf{c}^H(\nu) \right)^H \mathbf{F}_N \left[\widehat{\mathbf{W}}^* \odot \mathbf{Y} \right] \right) \right|^2 \\ &= \left| \text{tr} \left(\left(\mathbf{b}(\tau) \mathbf{c}^H(\nu) \right)^H \left(\mathbf{X}^* \odot \mathbf{F}_N \left[\widehat{\mathbf{W}}^* \odot \mathbf{Y} \right] \right) \right) \right|^2 \\ &= \left| \text{tr} \left(\mathbf{c}(\nu) \mathbf{b}^H(\tau) \left(\mathbf{X}^* \odot \mathbf{F}_N \left[\widehat{\mathbf{W}}^* \odot \mathbf{Y} \right] \right) \right) \right|^2 \\ &= \left| \text{tr} \left(\mathbf{b}^H(\tau) \left(\mathbf{X}^* \odot \mathbf{F}_N \left[\widehat{\mathbf{W}}^* \odot \mathbf{Y} \right] \right) \mathbf{c}(\nu) \right) \right|^2 \\ &= \left| \mathbf{b}^H(\tau) \left(\mathbf{X}^* \odot \mathbf{F}_N \left(\widehat{\mathbf{W}}^* \odot \mathbf{Y} \right) \right) \mathbf{c}(\nu) \right|^2, \end{aligned} \quad (80)$$

which, after being inserted into (79), results in (53).

APPENDIX E

CONVERGENCE ANALYSIS OF ALGORITHM 1

In this part, we provide the convergence analysis of the proposed ISAA algorithm in Algorithm 1 to identify the conditions under which the algorithm converges to a stationary point of the hybrid ML/MAP optimization problem in (38).

A. Formulation of Subproblems to Solve (38)

In Algorithm 1, we decompose the original problem (38) into two subproblems, each optimizing over either delay-Doppler or PN while keeping the other variable fixed in an alternating fashion. Let $(\hat{\tau}^{(i)}, \hat{\nu}^{(i)}, \hat{\xi}^{(i)})$ denote the delay, Doppler and PN estimates at the beginning of the i^{th} iteration of the alternating optimization procedure.

1) *Subproblem for PN Estimation:* The subproblem of (38) for PN estimation at the i^{th} iteration can be cast as

$$\widehat{\boldsymbol{\xi}}^{(i+1)} = \arg \min_{\boldsymbol{\xi}} \mathcal{L}(\widehat{\tau}^{(i)}, \widehat{\nu}^{(i)}, \boldsymbol{\xi}), \quad (81)$$

where $\mathcal{L}(\tau, \nu, \boldsymbol{\xi})$ is the hybrid ML/MAP objective function in (39). In the proposed ISAA approach, we tackle (81) by solving the equivalent problem

$$\widehat{\boldsymbol{\xi}}_{\Delta} = \arg \min_{\boldsymbol{\xi}_{\Delta}} \mathcal{L}(\widehat{\tau}^{(i)}, \widehat{\nu}^{(i)}, \boldsymbol{\xi}_{\Delta} + \widehat{\boldsymbol{\xi}}^{(i)}), \quad (82)$$

which estimates the residual PN $\boldsymbol{\xi}_{\Delta} = \boldsymbol{\xi} - \widehat{\boldsymbol{\xi}}^{(i)}$ in (40) instead of the actual PN $\boldsymbol{\xi}$ given the PN estimate $\widehat{\boldsymbol{\xi}}^{(i)}$ from the previous iteration. In the PN update step in Line 6 of Algorithm 1, the problem (81), or, equivalently (82), is solved in closed-form by applying the SAA for $\boldsymbol{\xi}_{\Delta}$:

$$e^{-j\boldsymbol{\xi}_{\Delta}} \approx \mathbf{1} - j\boldsymbol{\xi}_{\Delta}. \quad (83)$$

2) *Subproblem for Delay-Doppler Estimation:* The subproblem of (38) for delay-Doppler estimation at the i^{th} iteration is given by

$$(\widehat{\tau}^{(i+1)}, \widehat{\nu}^{(i+1)}) = \arg \min_{\tau, \nu} \mathcal{L}(\tau, \nu, \widehat{\boldsymbol{\xi}}^{(i+1)}). \quad (84)$$

The delay-Doppler update in Line 7 of Algorithm 1 finds an optimal solution of the problem (84).

B. Convergence Result

Based on the subproblem definitions in Sec. E-A, we can present the convergence result for Algorithm 1.

Proposition 1. *Assume that the SAA in (83) holds (i.e., the residual PN is small) and there exists a unique delay-Doppler pair that minimizes the objective in (84). Then, Algorithm 1, which solves (81) and (84) in an alternating fashion, converges to a stationary point of the hybrid ML/MAP optimization problem in (38).*

Proof. When the SAA in (83) holds, the closed-form solution given by (50) and (51) provides the optimal solution of the PN estimation subproblem in (81), or, equivalently (82), and is therefore a unique solution (being a closed-form one). Then, relying on the assumption that the solution to (84) is unique, it follows from [68, Proposition 1] that Algorithm 1 converges to a stationary point of (38).

APPENDIX F

COMPLEXITY ANALYSIS OF ALGORITHM 1

In this section, we analyze the per-iteration complexity of Algorithm 1. We first focus on the update of PN estimates via (50) and (51), and then study the complexity of updating delay-Doppler estimates via (53) and (54).

A. Complexity of PN Estimation in (50)–(51)

For convenience, we repeat the residual PN estimate in (50) here:

$$\widehat{\boldsymbol{\xi}}_{\Delta}(\tau, \nu) = -\mathbf{R}(\tau) \left(\Re \left\{ \boldsymbol{\Gamma}^{(i)}(\tau, \nu) \right\} \mathbf{R}(\tau) + \sigma^2 \mathbf{I} \right)^{-1} \times \left(\Im \left\{ \boldsymbol{\Gamma}^{(i)}(\tau, \nu) \right\} \mathbf{1} + \sigma^2 \mathbf{R}(\tau)^{-1} \widehat{\boldsymbol{\xi}}^{(i)} \right). \quad (85)$$

In the following, the complexity of (85) is analyzed in four steps.

1) *Complexity of $\mathbf{R}(\tau)^{-1} \widehat{\boldsymbol{\xi}}^{(i)}$:* For efficient computation of $\mathbf{R}(\tau)^{-1} \widehat{\boldsymbol{\xi}}^{(i)}$, the conjugate gradient (CG) method can be employed, similar to [29]. Note that computing

$$\mathbf{x} = \mathbf{R}(\tau)^{-1} \widehat{\boldsymbol{\xi}}^{(i)} \quad (86)$$

is equivalent to solving the following linear system of equations for \mathbf{x} [29]:

$$\mathbf{R}(\tau) \mathbf{x} = \widehat{\boldsymbol{\xi}}^{(i)}. \quad (87)$$

The CG method provides an iterative procedure to solve (87), where at each iteration, the major complexity results from a matrix-vector multiplication [29]

$$\boldsymbol{\omega} = \mathbf{R}(\tau) \boldsymbol{\kappa} \quad (88)$$

for some $\boldsymbol{\kappa} \in \mathbb{R}^{NM \times 1}$, where $\mathbf{R}(\tau) \in \mathbb{R}^{NM \times NM}$ is the PN covariance matrix given in (23).

Let us define $\boldsymbol{\omega} = [\boldsymbol{\omega}_0^T \dots \boldsymbol{\omega}_{M-1}^T]^T$ and $\boldsymbol{\kappa} = [\boldsymbol{\kappa}_0^T \dots \boldsymbol{\kappa}_{M-1}^T]^T$, where $\boldsymbol{\omega}_m \in \mathbb{R}^{N \times 1}$ and $\boldsymbol{\kappa}_m \in \mathbb{R}^{N \times 1}$ for each m . Then, using the Toeplitz-block Toeplitz structure of $\mathbf{R}(\tau)$ in (23), we can re-write (88) as

$$\boldsymbol{\omega}_m = \sum_{\ell=0}^{m-1} \mathbf{R}_{m-\ell}^T(\tau) \boldsymbol{\kappa}_{\ell} + \sum_{\ell=m}^{M-1} \mathbf{R}_{\ell-m}(\tau) \boldsymbol{\kappa}_{\ell} \quad (89)$$

for $m = 0, \dots, M-1$, where $\mathbf{R}_m(\tau) \in \mathbb{R}^{N \times N}$ is a Toeplitz matrix. Using the circulant approximation of Toeplitz matrices for large N [69], $\mathbf{R}_m(\tau)$ can be approximated as

$$\mathbf{R}_m(\tau) \approx \mathbf{R}_m^{\text{circ}}(\tau) = \mathbf{F}_N \boldsymbol{\Lambda}_m(\tau) \mathbf{F}_N^H, \quad (90)$$

where $\mathbf{F}_N \in \mathbb{C}^{N \times N}$ is the unitary DFT matrix, $\mathbf{R}_m^{\text{circ}}(\tau) \in \mathbb{R}^{N \times N}$ is the best circulant approximation to $\mathbf{R}_m(\tau)$ that minimizes $\|\mathbf{R}_m(\tau) - \mathbf{R}_m^{\text{circ}}(\tau)\|_F$ [69], and

$$\boldsymbol{\Lambda}_m(\tau) = \text{diag} \left(\sqrt{N} \mathbf{F}_N^H \mathbf{c}_m(\tau) \right) \in \mathbb{C}^{N \times N}, \quad (91)$$

with $\mathbf{c}_m(\tau)$ denoting the first column of $\mathbf{R}_m^{\text{circ}}(\tau)$.

Based on the approximation in (90), each summand in the second term of (89) can be expressed as

$$\mathbf{R}_{\ell-m}(\tau) \boldsymbol{\kappa}_{\ell} \approx \mathbf{F}_N \boldsymbol{\Lambda}_{\ell-m}(\tau) \mathbf{F}_N^H \boldsymbol{\kappa}_{\ell}, \quad (92)$$

which can be computed efficiently using FFT and IFFT, leading to $\mathcal{O}(N \log N)$ complexity. Similarly, for the summands in the first term of (89), we must compute

$$\mathbf{R}_{m-\ell}^T(\tau) \boldsymbol{\kappa}_{\ell} \approx \mathbf{F}_N^H \boldsymbol{\Lambda}_{m-\ell}(\tau) \mathbf{F}_N \boldsymbol{\kappa}_{\ell}, \quad (93)$$

which results in $\mathcal{O}(N \log N)$ complexity. In practice, as seen from the correlation characteristics of PN in Fig. 2, the PN correlation vanishes after a certain time lag, meaning that only a few blocks in $\mathbf{R}(\tau)$, say M_0 , are dominant in the computation of the right-hand side of (89) (i.e., $\mathbf{R}_0(\tau), \dots, \mathbf{R}_{M_0-1}(\tau)$), where $M_0 = 1$ for FROs due to the block-diagonal structure derived in Lemma 2 and $1 \leq M_0 \ll M$ for PLLs (typically, $M_0 \leq 3$). Hence, the complexity of (89) is given by

$$\mathcal{O}(M_0 N \log N), \quad (94)$$

which yields the following complexity for (88):

$$\mathcal{O}(M_0 M N \log N). \quad (95)$$

Assuming that the CG method requires I iterations to converge, the complexity of evaluating $\mathbf{R}(\tau)^{-1} \widehat{\boldsymbol{\xi}}^{(i)}$ in (86) can be expressed as

$$\mathcal{O}(I M_0 M N \log N). \quad (96)$$

2) *Complexity of $\Im \{ \Gamma^{(i)}(\tau, \nu) \} \mathbf{1}$* : Using the definition of $\Gamma^{(i)}(\tau, \nu)$ in (45), we can write

$$\begin{aligned} \Gamma^{(i)}(\tau, \nu) &= \left(\text{diag}(\mathbf{y})^H \mathbf{\Pi}_{\mathbf{q}(\tau, \nu)}^\perp \text{diag}(\mathbf{y}) \right) \odot \left(e^{-j\hat{\boldsymbol{\xi}}^{(i)}} (e^{j\hat{\boldsymbol{\xi}}^{(i)}})^T \right) \\ &= \left[\text{diag}(\mathbf{y})^H \text{diag}(\mathbf{y}) - \left(\mathbf{y}^* \mathbf{y}^T \odot \frac{\mathbf{q}(\tau, \nu) \mathbf{q}^H(\tau, \nu)}{\|\mathbf{q}(\tau, \nu)\|^2} \right) \right] \\ &\quad \odot \left(e^{-j\hat{\boldsymbol{\xi}}^{(i)}} (e^{j\hat{\boldsymbol{\xi}}^{(i)}})^T \right) \\ &= \text{diag}(|\mathbf{y}|^2) \\ &\quad - \frac{1}{\|\mathbf{q}(\tau, \nu)\|^2} \left(\mathbf{y}^* \odot \mathbf{q}(\tau, \nu) \odot e^{-j\hat{\boldsymbol{\xi}}^{(i)}} \right) \left(\mathbf{y}^* \odot \mathbf{q}(\tau, \nu) \odot e^{-j\hat{\boldsymbol{\xi}}^{(i)}} \right)^H \\ &= \text{diag}(|\mathbf{y}|^2) - \frac{1}{\|\mathbf{X}\|_F^2} \left(\mathbf{y}^* \odot \hat{\boldsymbol{\Xi}}^{(i)} \mathbf{q}(\tau, \nu) \right) \left(\mathbf{y}^* \odot \hat{\boldsymbol{\Xi}}^{(i)} \mathbf{q}(\tau, \nu) \right)^H \end{aligned} \quad (97)$$

where $\hat{\boldsymbol{\Xi}}^{(i)} \triangleq \text{diag} \left(e^{-j\hat{\boldsymbol{\xi}}^{(i)}} \right)$. Using (97), the real and imaginary parts of $\Gamma^{(i)}(\tau, \nu)$ are given by

$$\begin{aligned} \Re \left\{ \Gamma^{(i)}(\tau, \nu) \right\} &= \text{diag}(|\mathbf{y}|^2) \\ &\quad - \frac{1}{\|\mathbf{X}\|_F^2} \Re \left\{ \left(\mathbf{y}^* \odot \hat{\boldsymbol{\Xi}}^{(i)} \mathbf{q}(\tau, \nu) \right) \left(\mathbf{y}^* \odot \hat{\boldsymbol{\Xi}}^{(i)} \mathbf{q}(\tau, \nu) \right)^H \right\}, \\ \Im \left\{ \Gamma^{(i)}(\tau, \nu) \right\} &= -\frac{1}{\|\mathbf{X}\|_F^2} \Im \left\{ \left(\mathbf{y}^* \odot \hat{\boldsymbol{\Xi}}^{(i)} \mathbf{q}(\tau, \nu) \right) \left(\mathbf{y}^* \odot \hat{\boldsymbol{\Xi}}^{(i)} \mathbf{q}(\tau, \nu) \right)^H \right\}. \end{aligned} \quad (98)$$

Using (99), we can compute $\Im \{ \Gamma^{(i)}(\tau, \nu) \} \mathbf{1}$ as

$$\begin{aligned} \Im \left\{ \Gamma^{(i)}(\tau, \nu) \right\} \mathbf{1} &= -\frac{1}{\|\mathbf{X}\|_F^2} \Im \left\{ \left(\mathbf{y}^* \odot \hat{\boldsymbol{\Xi}}^{(i)} \mathbf{q}(\tau, \nu) \right) \left(\mathbf{y}^* \odot \hat{\boldsymbol{\Xi}}^{(i)} \mathbf{q}(\tau, \nu) \right)^H \mathbf{1} \right\}, \end{aligned} \quad (100)$$

which requires

$$\mathcal{O}(NM) \quad (101)$$

operations.

3) *Complexity of $\left(\Re \{ \Gamma^{(i)}(\tau, \nu) \} \mathbf{R}(\tau) + \sigma^2 \mathbf{I} \right)^{-1} \boldsymbol{\varpi}$* : Now that we have computed $\mathbf{R}(\tau)^{-1} \hat{\boldsymbol{\xi}}^{(i)}$ and $\Im \{ \Gamma^{(i)}(\tau, \nu) \} \mathbf{1}$ in (85), we will analyze the complexity of evaluating

$$\left(\Re \left\{ \Gamma^{(i)}(\tau, \nu) \right\} \mathbf{R}(\tau) + \sigma^2 \mathbf{I} \right)^{-1} \boldsymbol{\varpi}, \quad (102)$$

where

$$\boldsymbol{\varpi} = \Im \left\{ \Gamma^{(i)}(\tau, \nu) \right\} \mathbf{1} + \sigma^2 \mathbf{R}(\tau)^{-1} \hat{\boldsymbol{\xi}}^{(i)}. \quad (103)$$

Similar to the above analysis, the CG method can be employed to evaluate (102), where each iteration involves the computation of

$$\left(\Re \left\{ \Gamma^{(i)}(\tau, \nu) \right\} \mathbf{R}(\tau) + \sigma^2 \mathbf{I} \right) \boldsymbol{\kappa} \quad (104)$$

for some $\boldsymbol{\kappa} \in \mathbb{R}^{NM \times 1}$. Opening up the terms in (104), we have

$$\Re \left\{ \Gamma^{(i)}(\tau, \nu) \right\} \mathbf{R}(\tau) \boldsymbol{\kappa} + \sigma^2 \boldsymbol{\kappa}. \quad (105)$$

As previously derived in (95), evaluation of $\mathbf{R}(\tau) \boldsymbol{\kappa}$ in (105) has the complexity of

$$\mathcal{O}(M_0 MN \log N). \quad (106)$$

Next, defining $\boldsymbol{\omega} = \mathbf{R}(\tau) \boldsymbol{\kappa}$, we compute $\Re \{ \Gamma^{(i)}(\tau, \nu) \} \boldsymbol{\omega}$ in (105) using (98) as

$$\begin{aligned} \Re \left\{ \Gamma^{(i)}(\tau, \nu) \right\} \boldsymbol{\omega} &= \text{diag}(|\mathbf{y}|^2) \boldsymbol{\omega} \\ &\quad - \frac{1}{\|\mathbf{X}\|_F^2} \Re \left\{ \left(\mathbf{y}^* \odot \hat{\boldsymbol{\Xi}}^{(i)} \mathbf{q}(\tau, \nu) \right) \left(\mathbf{y}^* \odot \hat{\boldsymbol{\Xi}}^{(i)} \mathbf{q}(\tau, \nu) \right)^H \boldsymbol{\omega} \right\}, \end{aligned} \quad (107)$$

which leads to a complexity of $\mathcal{O}(NM)$. Combining this with (106), the complexity of computing the expression in (104) becomes

$$\mathcal{O}(M_0 MN \log N). \quad (108)$$

Finally, assuming I iterations for the CG method to converge, (102) has a computational complexity of

$$\mathcal{O}(IM_0 MN \log N). \quad (109)$$

4) *Final Complexity Result for (85)*: After evaluating (102), the final step to obtain (85) is to compute

$$\mathbf{R}(\tau) \boldsymbol{\varsigma}, \quad (110)$$

where

$$\boldsymbol{\varsigma} = \left(\Re \left\{ \Gamma^{(i)}(\tau, \nu) \right\} \mathbf{R}(\tau) + \sigma^2 \mathbf{I} \right)^{-1} \boldsymbol{\varpi}, \quad (111)$$

with $\boldsymbol{\varpi}$ being defined in (103). From (95), evaluation of (110) involves

$$\mathcal{O}(M_0 MN \log N) \quad (112)$$

operations. Combining (96), (101), (109) and (112), the computational complexity of (85) is obtained as

$$\mathcal{O}(IM_0 MN \log N). \quad (113)$$

B. Complexity of Delay-Doppler Estimation in (53)–(54)

To evaluate (54) in practice, it is enough to compute the first term as the remaining terms are negligibly small and can be discarded. We notice that the first term in (54) (up to a multiplicative constant)

$$\left| \mathbf{b}^H(\tau) \left(\mathbf{X}^* \odot \mathbf{F}_N(\widehat{\mathbf{W}}^* \odot \mathbf{Y}) \right) \mathbf{c}(\nu) \right|^2 \quad (114)$$

can be evaluated over a delay-Doppler grid via

$$\left| \mathbf{F}_N^H \left(\mathbf{X}^* \odot \mathbf{F}_N(\widehat{\mathbf{W}}^* \odot \mathbf{Y}) \right) \mathbf{F}_M \right|^2, \quad (115)$$

utilizing the fact that $\mathbf{b}(\tau)$ in (9) and $\mathbf{c}(\nu)$ in (10) correspond to DFT matrix columns for uniformly sampled delay-Doppler values. The complexity of (115) is thus given by

$$\mathcal{O}(NM) + \mathcal{O}(MN \log N) + \mathcal{O}(NM \log M), \quad (116)$$

where $\mathcal{O}(NM)$ is due to element-wise multiplication of $N \times M$ matrices, $\mathcal{O}(MN \log N)$ results from M times N -point FFT/IFFT, and $\mathcal{O}(NM \log M)$ comes from N times M -point FFT. Re-writing (116), the complexity of (115) can be expressed as

$$\mathcal{O}(NM \log(NM)). \quad (117)$$

C. Complexity of Algorithm 1

Using the complexity of PN estimation in (113) and that of delay-Doppler estimation in (117), the per-iteration complexity of Algorithm 1 can be written as

$$\mathcal{O}(MN (\log M + (IM_0 + 1) \log N)). \quad (118)$$

APPENDIX G
THEORETICAL GROUND FOR FORMULATION OF PN
EXPLOITATION PROBLEM IN (56)

In this section, we provide the theoretical motivation behind the parametric covariance matrix reconstruction problem in (56), which is formulated to resolve range ambiguity via PN exploitation. The goal of PN exploitation is to estimate the unknown delay τ from the PN estimate $\hat{\xi} \in \mathbb{R}^{NM \times 1}$ obtained at the output of Algorithm 1. Intuitively, this can lead to unambiguous estimates of τ since no ambiguity exists in PN covariance $\mathbf{R}(\tau)$ with respect to τ .

A. PN Observation Model and ML Estimator of Delay

The observation model for the above estimation problem can be written as

$$\hat{\xi} = \xi + \mathbf{n}, \quad (119)$$

where $\xi \in \mathbb{R}^{NM \times 1}$ denotes the true PN vector with $\xi \sim \mathcal{N}(\mathbf{0}, \mathbf{R}(\tau))$ and $\mathbf{n} \in \mathbb{R}^{NM \times 1}$ is the estimation noise, independent of ξ , whose statistics are given by $\mathbf{n} \sim \mathcal{N}(\mathbf{0}, \Sigma(\tau))$. Here, $\Sigma(\tau) \in \mathbb{R}^{NM \times NM}$ represents the covariance matrix of the PN estimation error in Algorithm 1 and can be set to the CRB matrix on PN estimation for the hybrid ML/MAP problem (38). Accordingly, the statistics of $\hat{\xi}$ in (119) are

$$\hat{\xi} \sim \mathcal{N}(\mathbf{0}, \mathbf{R}(\tau) + \Sigma(\tau)). \quad (120)$$

The ML estimator of τ from the PN estimates in (120) can be obtained as [70]

$$\hat{\tau} = \arg \min_{\tau} \left\{ \hat{\xi}^T (\mathbf{R}(\tau) + \Sigma(\tau))^{-1} \hat{\xi} + \log \det (\mathbf{R}(\tau) + \Sigma(\tau)) \right\}. \quad (121)$$

We identify several challenges in solving (121). First, the inverse of the covariance matrix of $\hat{\xi}$ needs to be calculated, which leads to a high computational burden. Second, only a single sample of PN estimate is available to solve (121), i.e., the sample covariance matrix $\hat{\xi} \hat{\xi}^T$ is rank-one, leading to poor estimates of τ . Additionally, the formulation in (121) does not allow us to exploit redundancy in $\mathbf{R}(\tau)$ stemming from its Toeplitz-block Toeplitz structure in (23).

B. Covariance Matching Approach

To overcome the aforementioned challenges, we propose a covariance matching (i.e., parametric covariance matrix reconstruction) approach that fits the sample covariance to the analytical model using a weighted least squares (WLS) formulation [66]:

$$\hat{\tau} = \arg \min_{\tau} \left\{ [\text{vec}(\hat{\mathbf{R}}) - \text{vec}(\mathbf{R}(\tau) + \Sigma(\tau))]^T (\hat{\mathbf{R}}^T \otimes \hat{\mathbf{R}})^{-1} \times [\text{vec}(\hat{\mathbf{R}}) - \text{vec}(\mathbf{R}(\tau) + \Sigma(\tau))] \right\}, \quad (122)$$

where $\hat{\mathbf{R}} = \hat{\xi} \hat{\xi}^T$ is the sample covariance matrix. By the extended invariance principle (EXIP), the proposed covariance matching based estimator (122) is asymptotically equivalent to the original ML estimator (121) at high SNRs [66]. Since $\hat{\mathbf{R}}$ is rank-one, $(\hat{\mathbf{R}}^T \otimes \hat{\mathbf{R}})$ is also rank-one and thus not invertible. Hence, we resort to the LS reformulation of (122):

$$\hat{\tau} = \arg \min_{\tau} \left\| \text{vec}(\hat{\mathbf{R}}) - \text{vec}(\mathbf{R}(\tau) + \Sigma(\tau)) \right\|^2. \quad (123)$$

C. High-SNR Approximation

The Toeplitz-block Toeplitz structure of $\mathbf{R}(\tau)$ cannot be exploited in (123) since $\Sigma(\tau)$ can have a generic covariance structure. Moreover, the sample covariance $\hat{\mathbf{R}}$ is constructed using a single observation $\hat{\xi}$ and thus constitutes a very inaccurate estimate of the true covariance $\mathbf{R}(\tau) + \Sigma(\tau)$. To deal with these issues, we propose to make the approximation

$$\mathbf{R}(\tau) + \Sigma(\tau) \approx \mathbf{R}(\tau), \quad (124)$$

which is valid at high SNRs since the CRB matrix elements are inversely proportional to SNR (i.e., PN estimation becomes sufficiently accurate at high SNRs such that $\mathbf{R}(\tau) + \Sigma(\tau)$ is dominated by the PN covariance $\mathbf{R}(\tau)$). By virtue of this high-SNR approximation, the problem (123) becomes

$$\hat{\tau} = \arg \min_{\tau} \left\| \text{vec}(\hat{\mathbf{R}}) - \text{vec}(\mathbf{R}(\tau)) \right\|^2, \quad (125)$$

which coincides with the formulation in (56). As seen from (57) and (58), the Toeplitz-block Toeplitz structure of $\mathbf{R}(\tau)$ can now be effectively exploited in (125) to estimate delay from a single observation of the PN vector.

REFERENCES

- [1] K. V. Mishra *et al.*, "Toward millimeter-wave joint radar communications: A signal processing perspective," *IEEE Signal Processing Magazine*, vol. 36, no. 5, pp. 100–114, Sep. 2019.
- [2] F. Liu *et al.*, "Joint radar and communication design: Applications, state-of-the-art, and the road ahead," *IEEE Transactions on Communications*, vol. 68, no. 6, pp. 3834–3862, 2020.
- [3] T. Wild *et al.*, "Joint design of communication and sensing for beyond 5G and 6G systems," *IEEE Access*, vol. 9, pp. 30 845–30 857, 2021.
- [4] D. Ma *et al.*, "Joint radar-communication strategies for autonomous vehicles: Combining two key automotive technologies," *IEEE Signal Processing Magazine*, vol. 37, no. 4, pp. 85–97, 2020.
- [5] J. A. Zhang *et al.*, "Enabling joint communication and radar sensing in mobile networks—a survey," *IEEE Communications Surveys Tutorials*, vol. 24, no. 1, pp. 306–345, 2022.
- [6] F. Liu *et al.*, "Integrated sensing and communications: Toward dual-functional wireless networks for 6G and beyond," *IEEE Journal on Selected Areas in Communications*, vol. 40, no. 6, pp. 1728–1767, 2022.
- [7] L. Zheng *et al.*, "Radar and communication coexistence: An overview: A review of recent methods," *IEEE Signal Processing Magazine*, vol. 36, no. 5, pp. 85–99, 2019.
- [8] A. Hassanien *et al.*, "Dual-function radar communication systems: A solution to the spectrum congestion problem," *IEEE Signal Processing Magazine*, vol. 36, no. 5, pp. 115–126, Sep. 2019.
- [9] F. Liu *et al.*, "Toward dual-functional radar-communication systems: Optimal waveform design," *IEEE Transactions on Signal Processing*, vol. 66, no. 16, pp. 4264–4279, Aug 2018.
- [10] J. Qian *et al.*, "Radar and communication spectral coexistence in range-dependent interference," *IEEE Transactions on Signal Processing*, vol. 69, pp. 5891–5906, 2021.
- [11] W. Saad *et al.*, "A vision of 6G wireless systems: Applications, trends, technologies, and open research problems," *IEEE Network*, vol. 34, no. 3, pp. 134–142, 2020.
- [12] C. Sturm *et al.*, "Waveform design and signal processing aspects for fusion of wireless communications and radar sensing," *Proceedings of the IEEE*, vol. 99, no. 7, pp. 1236–1259, July 2011.
- [13] M. Bică *et al.*, "Generalized multicarrier radar: Models and performance," *IEEE Transactions on Signal Processing*, vol. 64, no. 17, pp. 4389–4402, Sep. 2016.
- [14] F. Zhang *et al.*, "Joint range and velocity estimation with intrapulse and intersubcarrier Doppler effects for OFDM-based RadCom systems," *IEEE Transactions on Signal Processing*, vol. 68, pp. 662–675, 2020.
- [15] M. F. Keskin *et al.*, "Limited feedforward waveform design for OFDM dual-functional radar-communications," *IEEE Transactions on Signal Processing*, vol. 69, pp. 2955–2970, 2021.
- [16] A. Leshem *et al.*, "Phase noise compensation for OFDM systems," *IEEE Transactions on Signal Processing*, vol. 65, no. 21, pp. 5675–5686, 2017.
- [17] H. Wymeersch *et al.*, "Integration of communication and sensing in 6G: a joint industrial and academic perspective," in *2021 IEEE 32nd Annual International Symposium on Personal, Indoor and Mobile Radio Communications (PIMRC)*, 2021, pp. 1–7.
- [18] F. Bozorgi *et al.*, "RF front-end challenges for joint communication and radar sensing," in *1st IEEE Int. Online Symp. Joint Commun. Sens.*, Feb. 2021.

- [19] O. H. Salim *et al.*, "Channel, phase noise, and frequency offset in OFDM systems: Joint estimation, data detection, and hybrid cramer-rao lower bound," *IEEE Transactions on Communications*, vol. 62, no. 9, pp. 3311–3325, 2014.
- [20] M. F. Keskin *et al.*, "MIMO-OFDM joint radar-communications: Is ICI friend or foe?" *IEEE Journal of Selected Topics in Signal Processing*, vol. 15, no. 6, pp. 1393–1408, 2021.
- [21] M. Chung *et al.*, "Phase-noise compensation for OFDM systems exploiting coherence bandwidth: Modeling, algorithms, and analysis," *IEEE Transactions on Wireless Communications*, pp. 1–1, 2021.
- [22] D. D. Lin *et al.*, "The variational inference approach to joint data detection and phase noise estimation in OFDM," *IEEE Transactions on Signal Processing*, vol. 55, no. 5, pp. 1862–1874, 2007.
- [23] R. Wang *et al.*, "Channel estimation, carrier recovery, and data detection in the presence of phase noise in OFDM relay systems," *IEEE Transactions on Wireless Communications*, vol. 15, no. 2, pp. 1186–1205, 2016.
- [24] J. Rodríguez-Fernández, "Joint synchronization and compressive channel estimation for frequency-selective hybrid mmwave MIMO systems," *IEEE Transactions on Wireless Communications*, vol. 21, no. 1, pp. 548–562, 2022.
- [25] D. Petrovic *et al.*, "Effects of phase noise on OFDM systems with and without PLL: Characterization and compensation," *IEEE Transactions on Communications*, vol. 55, no. 8, pp. 1607–1616, 2007.
- [26] T. Schenk *et al.*, "On the influence of phase noise induced ICI in MIMO OFDM systems," *IEEE Communications Letters*, vol. 9, no. 8, pp. 682–684, 2005.
- [27] P. Mathecken *et al.*, "Performance analysis of OFDM with Wiener phase noise and frequency selective fading channel," *IEEE Transactions on Communications*, vol. 59, no. 5, pp. 1321–1331, 2011.
- [28] S. Wu *et al.*, "A phase noise suppression algorithm for OFDM-based WLANs," *IEEE Communications Letters*, vol. 6, no. 12, pp. 535–537, 2002.
- [29] D. D. Lin *et al.*, "Joint estimation of channel response, frequency offset, and phase noise in OFDM," *IEEE Transactions on Signal Processing*, vol. 54, no. 9, pp. 3542–3554, 2006.
- [30] Q. Zou *et al.*, "Compensation of phase noise in OFDM wireless systems," *IEEE Transactions on Signal Processing*, vol. 55, no. 11, pp. 5407–5424, 2007.
- [31] Z. Xue *et al.*, "OFDM radar and communication joint system using opto-electronic oscillator with phase noise degradation analysis and mitigation," *Journal of Lightwave Technology*, pp. 1–1, 2022.
- [32] B. Schweizer *et al.*, "On hardware implementations of stepped-carrier OFDM radars," in *2018 IEEE/MTT-S International Microwave Symposium - IMS*, 2018, pp. 891–894.
- [33] Z. Wei *et al.*, "Toward multi-functional 6G wireless networks: Integrating sensing, communication, and security," *IEEE Communications Magazine*, vol. 60, no. 4, pp. 65–71, 2022.
- [34] A. Tang *et al.*, "Self-interference-resistant IEEE 802.11ad-based joint communication and automotive radar design," *IEEE Journal of Selected Topics in Signal Processing*, vol. 15, no. 6, pp. 1484–1499, 2021.
- [35] Y. Zhuo *et al.*, "Multi-beam joint communication and radar sensing: Beamforming design and interference cancellation," *IEEE Communications Letters*, 2022.
- [36] P. Kumari *et al.*, "Adaptive and fast combined waveform-beamforming design for mmwave automotive joint communication-radar," *IEEE Journal of Selected Topics in Signal Processing*, vol. 15, no. 4, pp. 996–1012, 2021.
- [37] M. A. Uusitalo *et al.*, "6G vision, value, use cases and technologies for european 6G flagship project Hexa-X," *IEEE Access*, vol. 9, pp. 160004–160020, 2021.
- [38] R. F. Tigrek *et al.*, "OFDM signals as the radar waveform to solve Doppler ambiguity," *IEEE Transactions on Aerospace and Electronic Systems*, vol. 48, no. 1, pp. 130–143, Jan 2012.
- [39] M. Braun, "OFDM radar algorithms in mobile communication networks," *Karlsruher Institutes für Technologie*, 2014.
- [40] S. Mercier *et al.*, "Comparison of correlation-based OFDM radar receivers," *IEEE Transactions on Aerospace and Electronic Systems*, vol. 56, no. 6, pp. 4796–4813, 2020.
- [41] R. Xie *et al.*, "Performance analysis of joint range-velocity estimator with 2D-MUSIC in OFDM radar," *IEEE Transactions on Signal Processing*, vol. 69, pp. 4787–4800, 2021.
- [42] M. C. Budge *et al.*, "Range correlation effects in radars," in *The Record of the 1993 IEEE National Radar Conference*, April 1993, pp. 212–216.
- [43] A. R. Chiriyath *et al.*, "Joint radar-communications information bounds with clutter: The phase noise menace," in *2016 IEEE Radar Conference (RadarConf)*, May 2016, pp. 1–6.
- [44] M. Gerstmair *et al.*, "On the safe road toward autonomous driving: Phase noise monitoring in radar sensors for functional safety compliance," *IEEE Signal Processing Magazine*, vol. 36, no. 5, pp. 60–70, 2019.
- [45] C. Aydogdu *et al.*, "Radar interference mitigation for automated driving: Exploring proactive strategies," *IEEE Signal Processing Magazine*, vol. 37, no. 4, pp. 72–84, 2020.
- [46] S. Wu *et al.*, "OFDM systems in the presence of phase noise: consequences and solutions," *IEEE Transactions on Communications*, vol. 52, no. 11, pp. 1988–1996, 2004.
- [47] A. A. Nasir *et al.*, "Phase noise in MIMO systems: Bayesian Cramér–Rao bounds and soft-input estimation," *IEEE Transactions on Signal Processing*, vol. 61, no. 10, pp. 2675–2692, 2013.
- [48] A. Demir, "Computing timing jitter from phase noise spectra for oscillators and phase-locked loops with white and $1/f$ noise," *IEEE Transactions on Circuits and Systems I: Regular Papers*, vol. 53, no. 9, pp. 1869–1884, Sep. 2006.
- [49] A. Chorti *et al.*, "A spectral model for RF oscillators with power-law phase noise," *IEEE Transactions on Circuits and Systems I: Regular Papers*, vol. 53, no. 9, pp. 1989–1999, Sep. 2006.
- [50] J. Tao *et al.*, "Estimation of channel transfer function and carrier frequency offset for OFDM systems with phase noise," *IEEE Transactions on Vehicular Technology*, vol. 58, no. 8, pp. 4380–4387, 2009.
- [51] G. Hakobyan *et al.*, "A novel intercarrier-interference free signal processing scheme for OFDM radar," *IEEE Transactions on Vehicular Technology*, vol. 67, no. 6, pp. 5158–5167, 2017.
- [52] S. Bay *et al.*, "On the hybrid Cramér Rao bound and its application to dynamical phase estimation," *IEEE Signal Processing Letters*, vol. 15, pp. 453–456, 2008.
- [53] Y. Noam *et al.*, "Notes on the tightness of the hybrid Cramér–Rao lower bound," *IEEE Transactions on Signal Processing*, vol. 57, no. 6, pp. 2074–2084, 2009.
- [54] Z. Zhang *et al.*, "Full duplex techniques for 5G networks: self-interference cancellation, protocol design, and relay selection," *IEEE Communications Magazine*, vol. 53, no. 5, pp. 128–137, 2015.
- [55] P. Kumari *et al.*, "IEEE 802.11ad-based radar: An approach to joint vehicular communication-radar system," *IEEE Transactions on Vehicular Technology*, vol. 67, no. 4, pp. 3012–3027, April 2018.
- [56] C. B. Barneto *et al.*, "Full-duplex OFDM radar with LTE and 5G NR waveforms: Challenges, solutions, and measurements," *IEEE Transactions on Microwave Theory and Techniques*, vol. 67, no. 10, pp. 4042–4054, 2019.
- [57] A. Demir *et al.*, "Phase noise in oscillators: a unifying theory and numerical methods for characterization," *IEEE Transactions on Circuits and Systems I: Fundamental Theory and Applications*, vol. 47, no. 5, pp. 655–674, 2000.
- [58] P. Rabiei *et al.*, "A non-iterative technique for phase noise ICI mitigation in packet-based OFDM systems," *IEEE Transactions on Signal Processing*, vol. 58, no. 11, pp. 5945–5950, 2010.
- [59] X. Quan *et al.*, "Impacts of phase noise on digital self-interference cancellation in full-duplex communications," *IEEE Transactions on Signal Processing*, vol. 65, no. 7, pp. 1881–1893, 2017.
- [60] C. R. Berger *et al.*, "Signal processing for passive radar using OFDM waveforms," *IEEE Journal of Selected Topics in Signal Processing*, vol. 4, no. 1, pp. 226–238, 2010.
- [61] L. Zheng *et al.*, "Super-resolution delay-Doppler estimation for OFDM passive radar," *IEEE Transactions on Signal Processing*, vol. 65, no. 9, pp. 2197–2210, May 2017.
- [62] L. Gaudio *et al.*, "On the effectiveness of OTFS for joint radar parameter estimation and communication," *IEEE Transactions on Wireless Communications*, vol. 19, no. 9, pp. 5951–5965, 2020.
- [63] A. Murat *et al.*, "Phase-noise-induced performance limits for DPSK modulation with and without frequency feedback," *Journal of Lightwave Technology*, vol. 11, no. 2, pp. 290–302, 1993.
- [64] M. Wax *et al.*, "Efficient inversion of Toeplitz-block Toeplitz matrix," *IEEE Transactions on Acoustics, Speech, and Signal Processing*, vol. 31, no. 5, pp. 1218–1221, 1983.
- [65] P. Stoica *et al.*, "On reparametrization of loss functions used in estimation and the invariance principle," *Signal Processing*, vol. 17, no. 4, pp. 383–387, 1989.
- [66] B. Ottersten *et al.*, "Covariance matching estimation techniques for array signal processing applications," *Digital Signal Processing*, vol. 8, no. 3, pp. 185–210, 1998.
- [67] X. Du *et al.*, "Toeplitz structured covariance matrix estimation for radar applications," *IEEE Signal Processing Letters*, vol. 27, pp. 595–599, 2020.
- [68] A. Aubry *et al.*, "A new sequential optimization procedure and its applications to resource allocation for wireless systems," *IEEE Transactions on Signal Processing*, vol. 66, no. 24, pp. 6518–6533, 2018.
- [69] T. F. Chan, "An optimal circulant preconditioner for Toeplitz systems," *SIAM Journal on Scientific and Statistical Computing*, vol. 9, no. 4, pp. 766–771, 1988.
- [70] A. Swindlehurst *et al.*, "Maximum likelihood methods in radar array signal processing," *Proceedings of the IEEE*, vol. 86, no. 2, pp. 421–441, 1998.